

GPS/INS OPERATION IN SHADOWED ENVIRONMENTS

Except where reference is made to the work of others, the work described in this thesis is my own or was done in collaboration with my advisory committee. This thesis does not include proprietary or classified information.

Benjamin J. Clark

Certificate of Approval:

George T. Flowers
Professor
Mechanical Engineering

David M. Bevly, Chair
Assistant Professor
Mechanical Engineering

Andrew J. Sinclair
Assistant Professor
Aerospace Engineering

Joe F. Pittman
Interim Dean
Graduate School

GPS/INS OPERATION IN SHADOWED ENVIRONMENTS

Benjamin J. Clark

A Thesis

Submitted to

the Graduate Faculty of

Auburn University

in Partial Fulfillment of the

Requirements for the

Degree of

Master of Science

Auburn, Alabama
August 9, 2008

GPS/INS OPERATION IN SHADOWED ENVIRONMENTS

Benjamin J. Clark

Permission is granted to Auburn University to make copies of this thesis at its discretion, upon the request of individuals or institutions and at their expense. The author reserves all publication rights.

Signature of Author

Date of Graduation

VITA

Benjamin J. Clark was born in Athens, AL in February 1982. After living with his parents in Neil, AL, the Clark family returned to Athens where his parents still live. After graduating from East Limestone High School in 2000, he began attending Freed-Hardeman University where he met Follin Childs. Benjamin was awarded a B.S. in Mathematics in 2004 from Freed-Hardeman University. Just after their graduation, the couple were married and moved to Opelika, AL where Benjamin began work toward a B.S. in Mechanical Engineering at Auburn University. During these two years, he worked with Dr. David Bevly in the GPS and Vehicle Dynamics Laboratory. Upon completion of his undergraduate education, Benjamin entered graduate school in the summer of 2006.

THESIS ABSTRACT

GPS/INS OPERATION IN SHADOWED ENVIRONMENTS

Benjamin J. Clark

Master of Science, August 9, 2008
(B.S., Auburn University, 2006)
(B.S., Freed-Hardeman University, 2004)

111 Typed Pages

Directed by David Bevly

This thesis presents the analysis techniques developed for monitoring GPS signals in harsh shadowed environments such as heavy foliage. It also details a method selected for improved performance by combining raw GPS information with an Inertial Navigation System (INS). Normal GPS operation in shadowed areas suffer from position jumps of tens to hundreds of meters. The developed analysis reveals that these errors are due to the quickly changing local errors that cause a GPS receiver to report erroneous position spikes. Monitoring variables for the signal strength and change in multipath are employed to keep track of the environmental effects on the GPS measurements. A new visualization technique is also developed to qualitatively monitor the environmental effects.

From the visualization technique, the effects of the shadowing environment are shown to simultaneously affect the signal strength and multipath. It is shown that foliage cover causes these effects to occur spontaneously as a signal travels through and around obstacles. To mitigate these errors, a GPS/INS closely coupled system is implemented which uses inertial sensors to smooth the erroneous GPS jumps. Introduction of alternative sensors allows for integrity monitoring in the form of GPS outlier measurement rejection so

that local environmental effects can be detected and removed from the navigation solution. The resulting implementation reveals that it is possible to operate in these GPS harsh environments without suffering from the position jumps of tens or hundreds of meters. This implementation allows for navigation in foliage cover comparable to the under ten meter accuracy of standard GPS in clear environments.

ACKNOWLEDGMENTS

First and foremost, I am thankful to God for so many opportunities. I am thankful for my wife, Follin, who has put me through school here at Auburn University. I want to acknowledge my family in helping me to make learning a habit and my professors in equipping me with tools to follow that pursuit.

Style manual or journal used Journal of Approximation Theory (together with the style known as “aums”). Bibliography follows van Leunen’s *A Handbook for Scholars*.

Computer software used The document preparation package T_EX (specifically L^AT_EX) together with the departmental style-file `aums.sty`.

TABLE OF CONTENTS

LIST OF FIGURES	xii
LIST OF TABLES	xiv
1 INTRODUCTION	1
1.1 Objectives and Motivation	1
1.2 Prior Art	2
1.3 Contributions	4
1.4 Outline of Thesis	4
2 OVERVIEW OF GPS POSITION COMPUTATION	6
2.1 Nomenclature	6
2.2 Positioning Fundamentals	7
2.3 Satellites	9
2.3.1 Signals	9
2.3.2 GPS Control Segment	12
2.3.3 Ephemeris	13
2.4 Positioning	20
2.5 Summary	25
3 OVERVIEW OF GPS ERRORS	27
3.1 Satellite Errors	27
3.1.1 Errors in Ephemeris Data	28
3.1.2 Satellite Clock Errors	29
3.2 Atmospheric Errors	30
3.2.1 Ionospheric Errors	31
3.2.2 Tropospheric Errors	34
3.3 Local Errors	34
3.3.1 Multipath Error	34
3.3.2 Receiver Measurement Error	36
3.4 GPS Observable Error Models	37
3.5 Summary	37
4 SHADOWED ENVIRONMENTS	38
4.1 Environmental Error Monitoring Parameters	38
4.1.1 Signal Attenuation Monitoring Parameter	39
4.1.2 Multipath Monitoring Parameter	41

4.1.3	Error Visualization for a Single Satellite	43
4.1.4	Error Visualization for All Satellites in View	44
4.1.5	Analysis Results	45
4.2	Summary	47
5	ERROR MITIGATION	48
5.1	Differential Corrections	48
5.1.1	Position Differencing	49
5.1.2	Code Differencing	50
5.1.3	Carrier Smoothed Code Differencing	54
5.1.4	Static Comparison of Differential Methods	55
5.2	Inertial Aiding Sensors	56
5.2.1	Coupling Architectures	57
5.2.2	INS Mechanization Equations	58
5.2.3	State Vector	60
5.2.4	State Dynamics	61
5.2.5	State Measurement Relations	63
5.3	Fault Detection and Exclusion	67
5.3.1	Normalized Innovation Parameter	68
5.3.2	FDE Threshold	68
5.4	Summary	69
6	RESULTS	71
6.1	Pseudorange Calculated Position	71
6.2	Closely Coupled Implementation Results	75
6.3	Closely Coupled with FDE Implementation Results	76
6.4	Comparison of Methods	79
6.5	Summary	81
7	CONCLUSION	82
7.1	Future Work	83
	BIBLIOGRAPHY	85
	NOMENCLATURE	88
A	COORDINATE FRAMES AND TRANSFORMATIONS	90
A.1	Coordinate Frames	90
A.1.1	Earth-Centered Inertial (ECI) Frame	90
A.1.2	Earth-Centered Earth-Fixed (ECEF) Frame	91
A.1.3	Navigation Frame	91
A.1.4	Body Frame	92
A.1.5	Orbit Frame	92

A.1.6	Satellite Frame	95
A.2	Coordinate Transformations	95
A.2.1	Coordinate Transformation Matrix	95
A.3	ECEF and Geodetic Coordinates	96

LIST OF FIGURES

1.1	NovAtel Reported Position in Shadowed Environment	2
2.1	ECEF User Position	8
2.2	GPS Orbital Planes [20]	9
2.3	Orbit Angles	16
2.4	Position Using Least Squares Estimate	23
2.5	Position Using Weighted Least Squares Estimate	25
3.1	GPS Ephemeris Errors	29
3.2	Atmospheric Layers [3]	30
3.3	Typical Klobuchar Ionosphere Model [25]	33
3.4	Ionospheric Obliquity Factor Model [25]	33
3.5	Three Multipath Types	36
4.1	Illustration of GPS Signal Shadowing Due to Foliage	39
4.2	Static Data Collection Location	44
4.3	Single Satellite Error Visualization	45
4.4	Aerial View of Static Data Location	46
4.5	All-In-View Satellite Error Visualization	46
5.1	Common Satellite	50
5.2	Single Difference Diagram	51
5.3	Two Common Satellites	53

5.4	Method Comparison	55
5.5	Coupling Architectures	58
5.6	Fault Detection and Exclusion Threshold Selection	69
6.1	Dynamic Path	72
6.2	Clear Sky and Heavy Foliage Environments Along Dynamic Path	73
6.3	Pseudorange Calculated Positions	74
6.4	Zoom on Pseudorange Calculated Positions	74
6.5	Zoom on Closely Coupled Positions	76
6.6	Comparison of Closely Coupled and Pseudorange Solutions	77
6.7	Comparison of Closely Coupled with FDE and Pseudorange Solutions	77
6.8	Normalized Innovations Over Entire Path	78
6.9	Normalized Innovations Over Zoom Segment	78
6.10	Overlay of Positioning Methods In Heavy Foliage	79
6.11	Overlay of Positioning Methods In Clear Sky	80
6.12	Overlay of Positioning Methods In Light Foliage	80
A.1	Earth-Centered Inertial (ECI) Frame	91
A.2	Earth-Centered Earth-Fixed (ECEF) Frame	92
A.3	Navigation Frame	93
A.4	Body Frame	93
A.5	Orbital Plane With Respect To Equatorial Plane	94
A.6	Orbit Frame	94

LIST OF TABLES

2.1	Navigation Message Subframes	12
2.2	Clock and Ephemeris Parameters	14
2.3	Receiver Parameters from [24]	25
3.1	GPS Standard Error Budget [27]	27
4.1	Frequency-Lock-Loop Parameters from [36]	40
5.1	System Noise Covariance Matrix Values	63

CHAPTER 1

INTRODUCTION

1.1 Objectives and Motivation

The Global Positioning System (GPS) is gaining increased attention since reaching its full operational capability (FOC) in 1995 [21]. Although the system was designed for a user to navigate with a budget under \$10,000, user equipment prices have currently dropped below the \$100 mark and are continuing to drop as more capable computing resources are developed. Currently GPS navigation capabilities are found on aircraft, automobiles, cell phones, pets, and most any mobile user. These increasing navigation capabilities are leading to further advances in other fields. One such field is autonomous vehicle control, as can be seen by the use of GPS in the Darpa Grand Challenges [33]. With the global nature and long-term stability of GPS, such applications benefit from its use in being able to locate and orient a user accurately, consistently, and cheaply.

However, even with its prevalence and wide acceptance, there are certain applications for which stand-alone GPS does not meet the necessary performance requirements. One of these is navigation in signal-harsh environments such as areas around many tall buildings (urban canyon) or heavy tree cover. Much work has been done in investigating GPS operation in urban canyon environments, but significantly less has been done in evaluation of GPS operation in foliage cover. These foliage environments are described in the literature as shadowed environments and pose some unique difficulties to GPS operation [18]. An example of this operation is shown in Figure 1.1. This plot shows the position solutions reported by a NovAtel DL-3V GPS receiver in a rural subdivision with moderate foliage

cover. As can be observed, inaccurate position jumps of tens of meters can be seen as the receiver tries to operate in this signal-harsh environment.

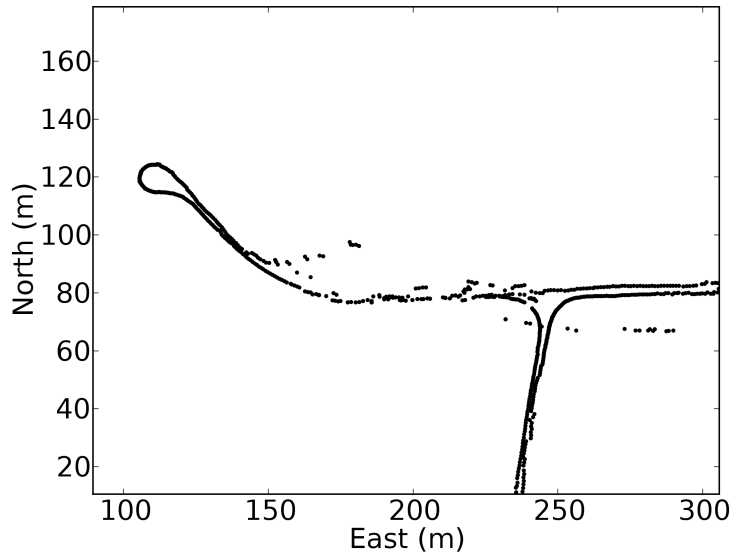


Figure 1.1: NovAtel Reported Position in Shadowed Environment

It is noted that such operation could lead to serious failures in a control system that uses such positions as the total navigation solution. Thus, the objective of this research is to analyze the cause of this performance degradation as well as ways to lessen its impact. The goal is a highly reliable system that performs well even in the aforementioned difficult environments.

1.2 Prior Art

Analysis of GPS operation has been investigated by several sources. Each of these studies had its own individual focus and target application. The use of GPS in measuring lengths of movement data was investigated in [10]. Here it was observed that the forest

canopy effects on GPS caused more position jumps and therefore a longer traveled distance was reported. Positioning errors were attributed to the canopy's interference with the satellite pseudoranges. Various forest cover types were studied in [38] with respect to their effect on GPS accuracy. In [16] a signal interruption probability (SIP) parameter was investigated in different forest conditions which was found to be related to the accuracy of carrier-phase differential operation in these environments. The link between integer ambiguity resolution and the SIP parameter was the main focus while the main effect monitored was the total loss of satellite tracking. In [30] the position dilution of precision (PDOP) value was investigated as a monitoring variable for operation in foliage environments. However, it was found that this geometry-based variable was not a good indicator of performance since a satellite that provided a good PDOP could be erroneous enough to make a solution worse than if it were ignored. In work done by Lachapelle, the multipath effect was studied as the main error source in foliage environments [22]. This work compares performance in foliage areas due to narrow or wide correlator spacing. This spacing corresponds to a receiver's ability to reject multipath, which is a large error contributor in these environments. A method for visualizing the multipath as a function of a satellite's azimuth and elevation was given in [17]. This technique yields impressive images describing the correlation of multipath over various regions around the receiver.

In order to operate in the foliage conditions, sensor integration has been investigated. A method proposed in [5] used a loosely coupled sensor fusion approach with GPS, gyroscope, encoders, and compass. This operation was implemented on a system with a human operator. To provide an increase in accuracy, a type of terrain-referencing was used by the operator of the robot. Steps were also taken to adjust the weighting on the measurements

through the measurement covariance matrix when jumps in the GPS solution occurred using a two meter threshold for detection.

1.3 Contributions

This thesis develops a detailed analysis of errors experienced by GPS users in shadowed environments. These errors include not only loss of tracking on the satellites but also their degradation even while still being available. This analysis includes the use of error monitoring variables capable of accurately describing the harsh effects of the foliage environment. A new visualization mechanism is also presented that allows for correlations between these monitoring variables to be qualitatively observed. With this analysis, system design conclusions are drawn for simplifying the implementation of a system to navigate in shadowed environments.

Also given are the details of an implemented system which combines GPS/INS coupling with an outlier rejection scheme. The coupling allows for continuous operation and more consistent results than stand-alone GPS. The rejection algorithm is a method of fault detection and exclusion (FDE) that increases the robustness of the navigation solution.

1.4 Outline of Thesis

Chapter 2 describes some background in GPS operation used throughout this thesis. Details are presented of how measurements are generated and how these measurements are used to calculate user position. Chapter 3 describes common errors that affect this solution experienced by all GPS users. These common errors arise from various sources and contribute to the overall error in the GPS measurements. Chapter 4 describes the shadowed

environment and the errors specific to such environments. The error monitoring variables are described and derived for analyzing the effectiveness of GPS in these environments. Then the visualization scheme is described and utilized for the improved navigation system design. Chapter 5 describes several error mitigation algorithms including differential operation and coupling with an inertial navigation system (INS). This chapter also describes the FDE algorithm used for systematic outlier rejection. Chapter 6 presents the results of the GPS/INS and FDE system. Finally, conclusions are presented in Chapter 7.

CHAPTER 2

OVERVIEW OF GPS POSITION COMPUTATION

Before delving into the details of the errors that affect GPS, some foundational information is presented. This chapter describes some of the basics a receiver uses to calculate a position using GPS observables. This includes the calculation of the satellite's position from broadcast ephemeris parameters as well as using these positions with measured ranges to the satellites. Also described are the various parts of the overall system that make positioning possible. This includes the satellites and GPS control segment, which oversees the satellite signals and position in space.

2.1 Nomenclature

In this thesis, a superscript represents the coordinate frame in which the components are reported. If a variable refers to a measure between two frame origins, a subscript is used with the frame the measure is from listed first and the frame the measure is to listed second. The frames mentioned in this paper are the inertial frame, i , the Earth-Centered-Earth-Fixed (ECEF) frame, e , the navigation frame, n , the body frame, b , the orbit frame, o , and the satellite frame, s . Detailed descriptions of these frames are provided in Appendix A and [14]. For example, the position of a user is taken to be the center of both the navigation and the body frames (which coincide but have different orientations). Therefore, expression of the user position in the ECEF frame would be expressed as r_{eb}^e . This is read as: position of the body frame origin with respect to the ECEF origin expressed in ECEF coordinates. The magnitude of a vector quantity is given without a coordinate frame in which the quantity

is reported in (no superscript). For example, the range from a user to a satellite is given as r_{bs} . Vector quantities that do not correspond with a single set of reference frames are denoted with an overbar. That is, the state vector would be labeled as \bar{x} .

2.2 Positioning Fundamentals

GPS is built upon several concepts, the first of which is time-ranging. If a radio signal is traveling at the known speed of light, c , and leaves its satellite source at a known time, t_s , a user can determine the range, r_{sb} , from the source by timing when the signal is measured, t_m , by

$$r_{sb} = c(t_m - t_s) \tag{2.1}$$

GPS position solutions can be calculated in an Earth-Centered Earth-Fixed (ECEF) frame, described in Appendix A. In this coordinate system, a user's position can be given by a longitude angle λ , a latitude angle ϕ , and a range r_{eb} . This situation is illustrated in Figure 2.1 and details of this transformation are given in Appendix A.

The second concept on which GPS is built is Euclidean distance. To calculate the geometric range between a user at $r_{eb}^e = (x_{eb}, y_{eb}, z_{eb})$ and a source (satellite) at $r_{es}^e = (x_{es}, y_{es}, z_{es})$, a user would apply the Euclidean distance formula

$$r_{bs} = \sqrt{(x_{es} - x_{eb})^2 + (y_{es} - y_{eb})^2 + (z_{es} - z_{eb})^2} \tag{2.2}$$

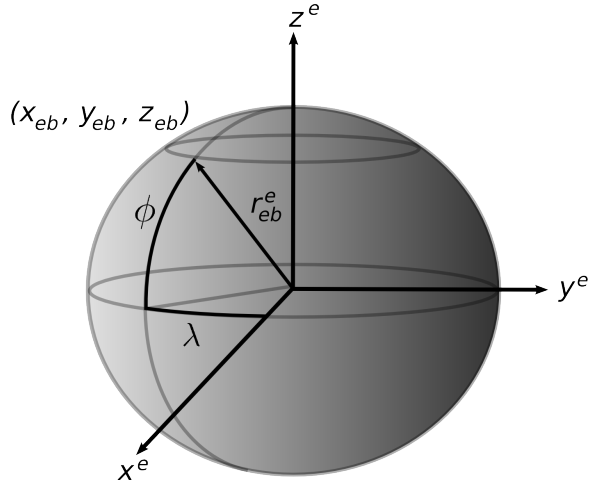


Figure 2.1: ECEF User Position

In the case of a GPS user, the range and the satellite position are known. Thus, multiple ranges are needed from multiple satellites in order to determine the user's position. Assuming the time is perfectly known by all satellites and the user, exactly three ranges are needed to solve for the user's ECEF position. However, the assumption that the user's clock is perfectly synchronized with GPS time used by the satellites is a poor one. Such systems would require expensive atomic clocks continuously running to keep track of this time. In order to reduce the required cost of user equipment, a clock bias state is also estimated along with the user's position. Thus a receiver needs to solve for four unknowns at a time to determine the correct position. Due to this fact, the range measurement is corrupted by the receiver's clock bias and various errors such as atmospheric delay and is therefore called a pseudorange measurement, ρ . For a satellite s , the overall pseudorange measurement model therefore becomes

$$\rho_s = \sqrt{(x_{es} - x_{eb})^2 + (y_{es} - y_{eb})^2 + (z_{es} - z_{eb})^2} + c\delta t_u + \epsilon_s \quad (2.3)$$

where δt_u is the user's clock offset error, $c\delta t_u$ is the user's clock bias in the units of meters, and ϵ_s is the pseudorange error for satellite s .

2.3 Satellites

There are currently 31 GPS satellites in orbit in 6 orbital planes [34]. The GPS constellation was originally designed with four satellites in each of these orbital planes with slots for spares [21]. The orbital planes described by the original design are shown in Figure 2.2. This design decision was to provide global availability and integrity, the details of which can be found in [20]. The constellation was designed to ensure users have the required minimum of 4 satellites in view for all users, neglecting local blockages.

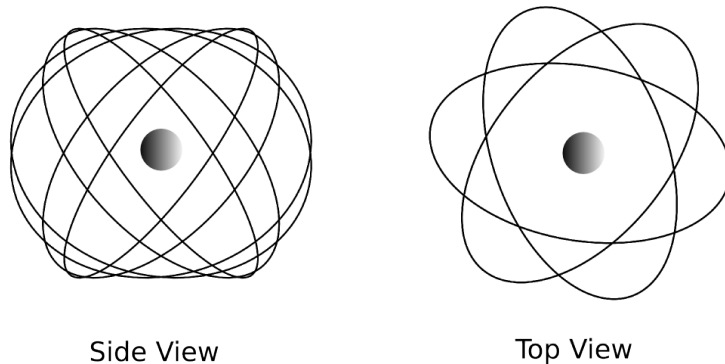


Figure 2.2: GPS Orbital Planes [20]

2.3.1 Signals

Each GPS satellite operates as a signal transmitter orbiting the earth every half of a sidereal day (11 hours 58 minutes) [21]. This implies that a user will see a satellite in approximately the same location at approximately the same time (4 minutes earlier) each

day. At a single full orbit, the observer will be on the opposite side of the Earth. This fact is an important consideration when taking into account repeatability in GPS experimentation. Each satellite uses a frequency synthesizer to drive subsystems generating three components of the signal: carrier, code, and navigation data message.

Carrier

The carrier subsystem generates the sinusoidal signals that center the frequency of the overall GPS signal. Currently all satellites (Block II/IIA/IIR/IIR-M) broadcast in the L-band at the L1 (1575.42 MHz) and the L2 (1227.6 MHz) frequencies. The satellites use other frequencies in the L-band and future implementations will include access on the L5 band (1176.45 MHz) [21]. The main design purpose of the carrier signals was to provide a means to effectively transmit the messages in the other subsystems. However, carrier phase measurements are also the basis of highly accurate positioning techniques when some of the inherent difficulties of the method are overcome. Since a receiver is capable of accurately measuring the carrier phase to a small fraction (about 1%) of the carrier wavelength, on the L1 signal this implies an accuracy of approximately 1.9 mm. This measurement is difficult to use since the whole number of wavelengths between the user and the satellite is not known. This problem is known as integer ambiguity. Techniques which solve a portion of this ambiguity between two receivers has had considerable research to utilize the carrier measurement for relative positioning between the receivers [23]. This technique is commonly referred to as Real-Time Kinematic (RTK) operation.

Code

The code subsystem includes two distinct set of code generators. These codes are used by the receiver to identify what satellites are available and also to determine the time of the signal arrival. Both codes are based on the same theory of maximal length codes and are chosen for their excellent autocorrelation and crosscorrelation properties. They are binary, deterministic, pseudo-random noise (prn) sequences that are distinct between any two satellites. The coarse-acquisition (C/A) code is modulated using binary phase shift keying (BPSK) onto the L1 carrier. It is a code that is 1023 bits (called chips for code sequences) long and repeats at a rate of 1.023 Mchips/s, or once every millisecond. The P(Y) code is a much longer code that is truncated after every 7-day period for a length of 6.1871×10^{12} chips at a rate of 10.23 Mchips/s. The increased frequency of the P(Y) code allows for more accurate measure of the signal time of arrival. This code is modulated onto both the L1 and L2 carriers but phase shifted 90° from the C/A code to avoid interference. The P(Y) code is currently encrypted for use only by US-government approved receivers and is not considered further in this thesis.

The special properties of these codes allow for the tracking of multiple satellites on the same carrier frequency, a property called code-division multiple access (CDMA). A receiver can generate a local replica of the code and multiply the incoming signal with this local replica to track and determine time of arrival.

Navigation Message

The last signal subsystem generates the navigation message. This is a 50 bit/s message that includes all the data parameters needed by the receiver to calculate a satellite's position

(called ephemeris), health, clock correction, and other items as well as the GPS week, time, etc. The navigation message was designed to transmit a large amount of data efficiently while maintaining a relatively slow bit rate. Each frame of the navigation message is broken into five subframes, the contents of which are shown in Table 2.1 [19].

Table 2.1: Navigation Message Subframes

Subframe	Contents
1	Clock Correction & Satellite Quality
2	Ephemeris
3	Ephemeris
4	Almanac & Ionosphere & UTC Correction
5	Almanac

2.3.2 GPS Control Segment

The GPS control segment tracks the progress of the satellites and uses their measurements to estimate health, clock errors, path, etc. Parameters are then formed and an uplink loads the desired parameters back onto the satellites to be broadcasted to the users through the navigation message.

The GPS control segment consists of 4 control stations capable of relaying updated information to the satellites, 6 monitor stations to track the satellite’s progress, and 10 National Geospatial-Intelligence Agency (NGA) tracking stations [21]. The increasing number of sites in use has several benefits to the overall system. First, the control segment is better capable of detecting errors in the individual satellites which leads to quicker response to gross failure detection and user warning. This warning can be issued by the control segment by switching the satellite’s status from healthy to not recommended for use. Secondly, increased tracking capabilities have led to improved path estimation for the satellites. With

better knowledge of the path, more accurate ephemeris parameters can be transmitted to the users. This improvement has led to the general user's improved positioning accuracy as well [8].

2.3.3 Ephemeris

For the user to calculate his position, he must have measured ranges from at least four satellites for reasons explained in Section 2.2. The receiver must also be able to determine the position of the range source (i.e. the satellite) at the time of position calculation. This is accomplished by reading the ephemeris parameters from the navigation message transmitted by the satellites.

The ephemeris parameters are actually estimated Keplerian orbit parameters along with other parameters that define corrections to Kepler's motion model. These parameters are listed and described in Table 2.2, which is taken from [11].

Satellite Clock Correction

Part of the ephemeris parameters are used by the receiver to calculate the satellite's clock error. Although the atomic clocks aboard the space vehicles are highly accurate and stable, using them without correction would lead to a large degradation in accuracy. By using Equation (2.1), it is seen that the transit time, t_t , (time the signal took to go from the satellite to the receiver) and the transmission time, t_s , are

$$t_t = t_m - t_s = \frac{r_u}{c} \approx \frac{\rho_u}{c} \quad (2.4)$$

$$t_s = t_m - \frac{\rho_u}{c} \quad (2.5)$$

Table 2.2: Clock and Ephemeris Parameters

Parameter	Description	Units
T_{GD}	Group Delay	s
IODC	Issue of data, clock	-
t_{oc}	Clock data reference time	s
a_{f2}	Second-order correction to the satellite clock	s/s ²
a_{f1}	First-order correction to the satellite clock	s/s
a_{f0}	Constant correction to the satellite clock	s
M_0	Mean anomaly at reference time	semicircles
Δ_n	Mean motion difference from computed value	semicircles
e	Eccentricity	-
\sqrt{A}	Square root of the semimajor axis	$\sqrt{\text{m}}$
$\Delta\Omega_0$	Right ascension at reference time	semicircles
i_0	Inclination angle at reference time	semicircles
ω	Argument of perigee	semicircles
$\Delta\dot{\Omega}$	Rate of right ascension	semicircles/s
$\Delta\dot{i}$	Rate of inclination angle	semicircles/s
C_{uc}	Cosine harmonic correction term to the argument of latitude	rad
C_{us}	Sine harmonic correction term to the argument of latitude	rad
C_{rc}	Cosine harmonic correction term to the orbit radius	m
C_{rs}	Sine harmonic correction term to the orbit radius	m
C_{ic}	Cosine harmonic correction term to the angle of inclination	rad
C_{is}	Sine harmonic correction term to the angle of inclination	rad
t_{oe}	Ephemeris reference time	s
IODE	Issue of data, ephemeris	-

All of the above variables are either known or measured. The satellite clock error is modeled as a quadratic function with parameters a_{f0} , a_{f1} , and a_{f2} . They are available from the navigation message in subframe 1 shown in Table 2.1. It is used in function form with time referenced from the clock correction reference time, t_{oc} . The clock correction is calculated as

$$dt_{sv} = a_{f0} + a_{f1}(t_s - t_{oc}) + a_{f2}(t_s - t_{oc})^2 + dt_r - T_{GD} \quad (2.6)$$

where T_{GD} is the group delay clock correction for single frequency users (L1 or L2 only). This is necessary since the clock delay cannot be corrected without dual frequency use [7]. Also, dt_r is a relativistic correction term calculated as

$$dt_r = Fe\sqrt{A} \sin(E_k) \quad (2.7)$$

where the orbit parameters, e , A , and E_k , are described in the satellite position section and F is a constant whose value is $-4.442807633 \times 10^{-10}$ s/ $\sqrt{\text{m}}$ [7]. The user can calculate the corrected transmission time with the satellite clock correction and therefore the time from the ephemeris reference epoch (t_{oe}) as

$$t = t_s - dt_{sv} \quad (2.8)$$

$$t_k = t - t_{oe} \quad (2.9)$$

The time from the ephemeris reference epoch is defined to account for beginning or ending of week crossovers. The logic to account for the crossover is that if the value is greater than 302,400 s, then 604,800 s are subtracted from it. Likewise, if the value is less than -302,400 s, then 604,800 s are added to it. This approach tracks the time difference since the value of t is reset at the start of a new GPS week [7].

Satellite Position

Determining where a satellite is in its orbit amounts to finding the angle it is from the orbit's perigee (point of closest approach to the Earth). This angle is the eccentric anomaly and is shown in Figure 2.3 as E . The mean anomaly, M , is used due to the highly

nonlinear change of speed of a body in orbit and the corresponding difficulty in calculating the angle traveled over time. The mean anomaly has a range between 0 and 2π . This value is also shown in Figure 2.3 and allows for a linear relation between angles along an auxiliary circle versus time and is calculated by time-scaling the mean motion parameter n , shown in Equation (2.11).

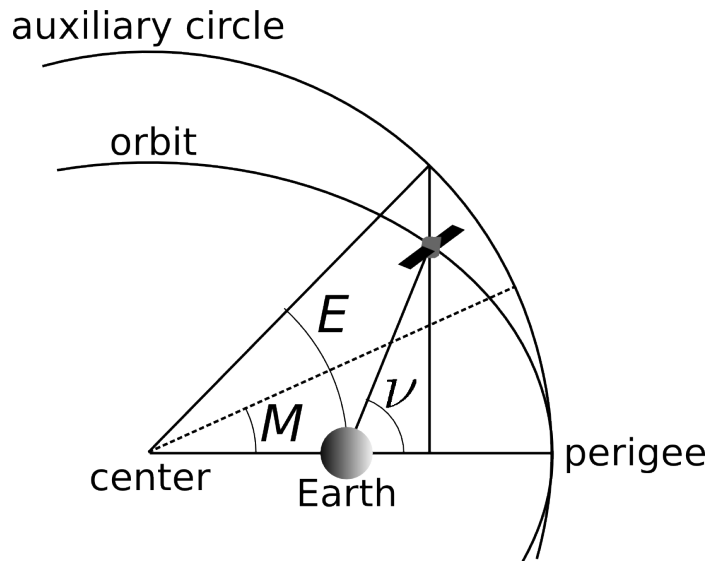


Figure 2.3: Orbit Angles

Using the ephemeris parameters described in Table 2.2, the satellite position can be calculated. The mean motion parameter is calculated as

$$n = \Delta_n + \bar{\omega}_{is} \quad (2.10)$$

where $\bar{\omega}_{is} = \sqrt{\mu/a^3}$ and μ is the Earth's gravitational constant, which has a value of $3.986004418 \times 10^{14} \text{m}^3/\text{s}^2$ according to the WGS84 standard [14]. The mean anomaly is an

angular measure that is linear with time and is calculated as

$$M = M_0 + t_k n \quad (2.11)$$

With this value, the eccentric anomaly, E , is solved iteratively until convergence using Kepler's equation

$$E = M + e \sin(E) \quad (2.12)$$

Similarly, E will have a value within the range of 0 and 2π . With the eccentric anomaly, the true anomaly, ν , can be found as

$$\nu = \tan^{-1} \left(\frac{\frac{\sqrt{1-e^2} \sin(E)}{1-e \cos(E)}}{\frac{\cos(E)-e}{1-e \cos(E)}} \right) \quad (2.13)$$

where \tan^{-1} refers to the four-quadrant inverse tangent. Next the argument of latitude, Φ , can be calculated to lie within the range of 0 and 2π as

$$\Phi = \nu + \omega \quad (2.14)$$

Using the C terms from the ephemeris parameters in Table 2.2, corrections for the argument of latitude, radius, and inclination can be calculated as

$$\delta u_{os}^o = C_{us} \sin(2\Phi) + C_{uc} \cos(2\Phi) \quad (2.15)$$

$$\delta r_{os}^o = C_{rs} \sin(2\Phi) + C_{rc} \cos(2\Phi) \quad (2.16)$$

$$\delta i = C_{is} \sin(2\Phi) + C_{ic} \cos(2\Phi) \quad (2.17)$$

$$u_{os}^o = \Phi + \delta u_{os}^o \quad (2.18)$$

$$r_{os}^o = A(1 - e \cos(E)) + \delta r_{os}^o \quad (2.19)$$

$$i = i_0 + \delta i + \Delta \dot{i} t_k \quad (2.20)$$

Now the 2D position in the orbital plane can be found as

$$x_{os}^o = r_{os}^o \cos(u_{os}^o) \quad (2.21)$$

$$y_{os}^o = r_{os}^o \sin(u_{os}^o) \quad (2.22)$$

The correction to the ascending node Ω , which is the angle determining where the orbit crosses the Earth, can then be calculated to be within 0 to 2π as

$$\Omega = \Omega_0 + (\dot{\Omega} - \Omega_e) t_k - \Omega_e (t_{oe} + t_t + dt_{sv}) \quad (2.23)$$

With these values, the ECEF position of the satellite at time t_s can be calculated as

$$x_{es}^e = x_{os}^o \cos(\Omega) - y_{os}^o \cos(i) \sin(\Omega) \quad (2.24)$$

$$y_{es}^e = x_{os}^o \sin(\Omega) + y_{os}^o \cos(i) \cos(\Omega) \quad (2.25)$$

$$z_{es}^e = y_{os}^o \sin(i) \quad (2.26)$$

Satellite Velocity

For some processing procedures, the satellite velocity is also required. A numerical approximation to this value can be generated by calculating the satellite positions at two successive times and dividing by the time difference in the two epoch. Assuming the time

difference is a sufficiently small value, this value can be used as the satellite velocity. Alternatively, the orbit Equations 2.10 thru 2.26 can be differentiated to get an analytical solution for satellite velocity [14].

$$\dot{E} = \frac{\bar{\omega}_{is} + \Delta_n}{1 - e \cos(E)} \quad (2.27)$$

$$\dot{\Phi} = \frac{\sin(\nu)}{\sin(E)} \dot{E} \quad (2.28)$$

$$\dot{r}_{os}^o = Ae \sin(E) \dot{E} + 2(C_{rs} \cos(2\Phi) - C_{rc} \sin(2\Phi)) \dot{\Phi} \quad (2.29)$$

$$\dot{u}_{os}^o = (1 + 2C_{us} \cos(2\Phi) - 2C_{uc} \sin(2\Phi)) \dot{\Phi} \quad (2.30)$$

Therefore the time derivative of the satellite's orbit coordinates are

$$\dot{x}_{os}^o = \dot{r}_{os}^o \cos(u_{os}^o) - r_{os}^o \dot{u}_{os}^o \sin(u_{os}^o) \quad (2.31)$$

$$\dot{y}_{os}^o = \dot{r}_{os}^o \sin(u_{os}^o) + r_{os}^o \dot{u}_{os}^o \cos(u_{os}^o) \quad (2.32)$$

The changes in the ascending node and inclination are calculated as

$$\dot{\Omega} = \dot{\bar{\Omega}} - \Omega_e \quad (2.33)$$

$$\dot{i} = \dot{\Delta i} + 2(C_{is} \cos(2\Phi) - C_{ic} \sin(2\Phi)) \dot{\Phi} \quad (2.34)$$

Thus the satellite ECEF velocity is found as

$$\begin{aligned} \dot{x}_{es}^e &= \dot{x}_{os}^o \cos(\Omega) - \dot{y}_{os}^o \cos(i) \sin(\Omega) + \dot{y}_{os}^o \sin(i) \sin(\Omega) \\ &\quad + \left(\Omega_e - \dot{\Omega}\right) (x_{os}^o \sin(\Omega) + y_{os}^o \cos(i) \cos(\Omega)) \end{aligned} \quad (2.35)$$

$$\begin{aligned} \dot{y}_{es}^e &= \dot{x}_{os}^o \sin(\Omega) + \dot{y}_{os}^o \cos(i) \cos(\Omega) - \dot{y}_{os}^o \sin(i) \cos(\Omega) \\ &\quad + \left(\Omega_e - \dot{\Omega}\right) (-x_{os}^o \cos(\Omega) + y_{os}^o \cos(i) \sin(\Omega)) \end{aligned} \quad (2.36)$$

$$\dot{z}_{es}^e = \dot{y}_{os}^o \sin(i) - \dot{y}_{os}^o \cos(i) \quad (2.37)$$

2.4 Positioning

Four satellites are required to determine a user's position with reasonable accuracy with the four unknowns of user ECEF position and clock bias, $(x_u, y_u, z_u, c\delta t_u)$. Additional satellites allow for an overdetermined solution and other techniques, to be discussed in subsequent chapters, make use of this situation. Several hand-held GPS receivers allow an additional constraint of being on the Earth's surface to remove altitude as an unknown. This approach only requires three satellites to determine two position coordinates along with the receiver's clock bias [13]. However, this is often a poor assumption as local height changes relative to the Earth geoid are difficult to account for, and the user may violate this constraint.

Considering a single time epoch, the user's state vector \bar{X} is made up of the receiver's ECEF position r_{eb}^e and clock bias in range form $c\delta t_u$.

$$\bar{X} = \begin{bmatrix} x_{eb} \\ y_{eb} \\ z_{eb} \\ c\delta t_u \end{bmatrix} \quad (2.38)$$

The measurement vector at this epoch is generated by placing all available pseudorange measurements in a column vector for all m satellites being tracked,

$$\bar{Y} = \begin{bmatrix} \rho_1 \\ \vdots \\ \rho_m \end{bmatrix} \quad (2.39)$$

The observation-state relationships are found by placing the right sides of Equation (2.3) into vector form so that

$$\bar{G} = \begin{bmatrix} \sqrt{(x_1 - x_u)^2 + (y_1 - y_u)^2 + (z_1 - z_u)^2} + c\delta t_u \\ \vdots \\ \sqrt{(x_m - x_u)^2 + (y_m - y_u)^2 + (z_m - z_u)^2} + c\delta t_u \end{bmatrix} \quad (2.40)$$

To efficiently solve this set of equations for the state, linearization is used to change the problem into a recursively solved system. The linearization is taken about point \bar{X}^* and a state correction vector is defined as

$$\bar{x} = \bar{X} - \bar{X}^* \quad (2.41)$$

Using Taylor series expansion on Equation (2.40) and neglecting higher order non-linear terms yields

$$\begin{aligned}
\bar{Y} &\approx \bar{G}|_{\bar{X}^*} + \left. \frac{\partial \bar{G}}{\partial \bar{X}} \right|_{\bar{X}^*} \bar{x} \\
&= \bar{Y}^* + H\bar{x} \\
&= \begin{bmatrix} \rho_1^* \\ \vdots \\ \rho_m^* \end{bmatrix} + \begin{bmatrix} -(\bar{e}_{u1}^*)^T & 1 \\ \vdots & \vdots \\ -(\bar{e}_{um}^*)^T & 1 \end{bmatrix} \bar{x}
\end{aligned} \tag{2.42}$$

where ρ^* represents the estimated pseudorange using the linearization point as the user's ECEF position and clock bias and \bar{e}_{us}^* represents the unit vector from the user to the satellite. It is determined by

$$\bar{e}_{us}^* = \begin{bmatrix} \frac{x_u^* - x_s}{r_s^*} \\ \frac{y_u^* - y_s}{r_s^*} \\ \frac{z_u^* - z_s}{r_s^*} \end{bmatrix} \tag{2.43}$$

Therefore a measurement correction vector is calculated as

$$\bar{y} = \bar{Y} - \bar{Y}^* = H\bar{x} \tag{2.44}$$

A least-squares solution to Equation (2.44) minimizes the error between the measurement correction and the transformed state correction according to a cost function, where the error is defined as

$$\epsilon = \bar{y} - H\bar{x} \tag{2.45}$$

In the case of least-squares, this cost function is

$$J_{LS} = \epsilon^T \epsilon \quad (2.46)$$

Thus, it minimizes the sum of the squared error. The solution of this problem is well documented in several sources [31, 32] and is calculated as the solution to

$$\left(H^T H\right) \hat{x} = H^T \bar{y} \quad (2.47)$$

Methods to solve this system include the pseudoinverse, decomposition, etc. The result of this least-squares solution method on a typical set of static data is shown below in Figure 2.4. Notice in this figure that this method yields jumps approximately tens of meters from the mean position. The source of these errors will be discussed in Chapter 3.

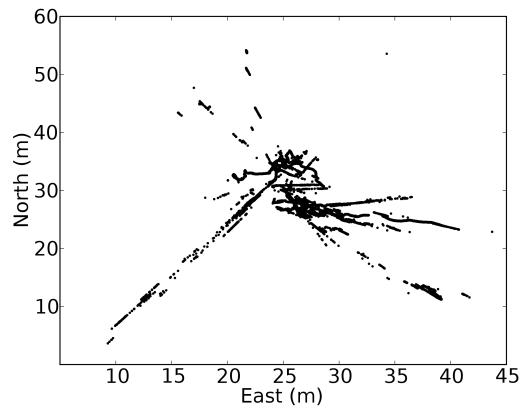


Figure 2.4: Position Using Least Squares Estimate

An improved solution can be found by using a weighted least squares method if variance information is available for each measurement [32]. In this method, the variances for each pseudorange measurement are placed along the diagonal of a covariance matrix R . Using

these weights changes the cost function to be

$$J_{WLS} = \epsilon^T R^{-1} \epsilon \quad (2.48)$$

The resulting minimization gives the relation

$$\left(H^T R^{-1} H\right)^{-1} H^T \hat{x} = R^{-1} \bar{y} \quad (2.49)$$

Similar methods used to solve Equation 2.47 can be used to solve Equation 2.49.

As will be described later in Chapter 3, many of the errors that affect a GPS receiver have been well studied and their variances described in the literature [27]. Major error sources affecting a well placed static receiver are atmosphere errors and receiver errors. The overall pseudorange variance can be approximated as

$$\sigma_\rho^2 = \sigma_{tDLL}^2 + \sigma_{atm}^2 \quad (2.50)$$

where σ_{tDLL}^2 is the thermal noise variance of the receiver's delay locked loop, which generates the pseudorange measurements, and σ_{atm}^2 is the variance of the atmospheric effects on the pseudorange measurement. Taking the total effect of the ionospheric and tropospheric error gives a variance approximated as $\sigma_{atm}^2 = 5.22$ [24]. The thermal noise variance of the receiver's delay locked loop is shown as a function of the carrier to noise ratio C/N_0 as shown in Equation 2.51 [24].

$$\sigma_{tDLL} = \lambda_c \sqrt{\frac{4F_1 d^2 B_n}{C/N_0} \left(2(1-d) + \frac{4F_2 d}{TC/N_0} \right)} \quad (2.51)$$

The description of the receiver specific terms are given in Table 2.3 along with values taken from [24]. Using this variance, an example set of position solutions is shown in Figure 2.5.

Table 2.3: Receiver Parameters from [24]

Parameter	Description	Value	Units
F_1	discriminator correlator factor	1	-
F_2	discriminator type factor	1	-
d	correlator spacing	1/2	chips
B_n	code loop noise bandwidth	2	Hz
T	prediction integration time	2	ms
λ_c	code chipping rate	293.05	chips/s

Compared to solutions shown in Figure 2.4, this method produces a less noisy and more accurate position solution by de-weighting pseudoranges that are comparatively weak (low C/N_0 values).

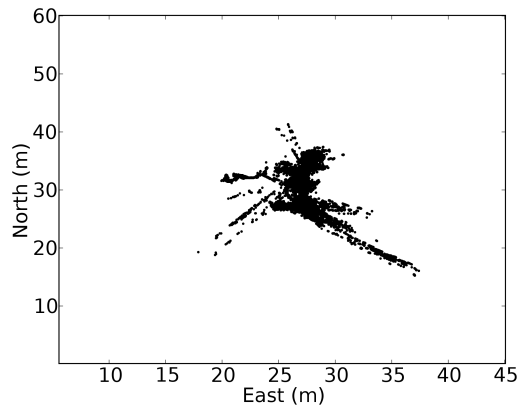


Figure 2.5: Position Using Weighted Least Squares Estimate

2.5 Summary

This chapter describes the basics necessary for a GPS receiver to calculate its position using the ephemeris parameters from the GPS data message and the pseudoranges found

from determining the difference in transmission time, t_s , and the user's measurement time t_u . Chapter 3 will build on this background and show the effects of various error sources on GPS operation.

CHAPTER 3

OVERVIEW OF GPS ERRORS

Much work has been done in analyzing the errors in GPS since its use began. A central source of information could be considered [27], which details the major error sources and includes a commonly quoted error budget, shown in Table 3.1. Several error modes have been heavily studied when it comes to the use of GPS receivers. They are typically grouped into three different error regions: satellite, atmospheric, and local. The satellite errors are the ephemeris data and satellite clock errors. The atmospheric errors are the ionosphere and troposphere delays. Finally, the local errors are the multipath and receiver measurement errors.

Table 3.1: GPS Standard Error Budget [27]

Error source	One-sigma error, m		
	Bias	Random	Total
Ephemeris data	2.1	0.0	2.1
Satellite clock	2.0	0.7	2.1
Ionosphere	4.0	0.5	4.0
Troposphere	0.5	0.5	0.7
Multipath	1.0	1.0	1.4
Receiver measurement	0.5	0.2	0.5
UERE, rms	5.1	1.4	5.3
Filtered UERE, rms	5.1	0.4	5.1

3.1 Satellite Errors

The GPS constellation was engineered to provide high accuracy position using ranges from the satellites. As with all implementations, there are still errors that must be accounted for. The errors in this section deal with the design and implementation of the satellites.

Both of these error sources have broadcast correction models that significantly decrease their effect, but there are still unmodeled effects that affect the user in navigation calculations. These errors are the same for all users of GPS and therefore are exactly correlated between any two locations. This fact can be used in certain error mitigation techniques described later.

3.1.1 Errors in Ephemeris Data

The satellite positions are not perfectly known to the user. To determine a satellite's position in ECEF coordinates, the user receives the satellite's ephemeris parameters in the navigation message. These parameters define the satellite's path estimated by the GPS control segment. This path is evaluated at the time the signal leaves the satellite's antenna. Since this path is an estimate, there is a difference between the true satellite path and the path described by the ephemeris parameters. These errors are typically 3-5 m rms [25]. However, most of this error is in the cross-track direction which means it affects the direction to the satellite rather than the range, as shown in Figure 3.1. Errors in the direction to the satellite (which arise in the unit vector from the user to the satellite) have a much smaller impact than along-track errors [27]. The resulting ranging error from the satellite's position is therefore on the order of 1.5 m. The orbit model is updated by the GPS control segment periodically (anywhere from about eight hours to daily). At the time of update, the ephemeris error is nearly zero since the time is near the reference time for the orbit. As time progresses between ephemeris updates, the satellite position error grows.

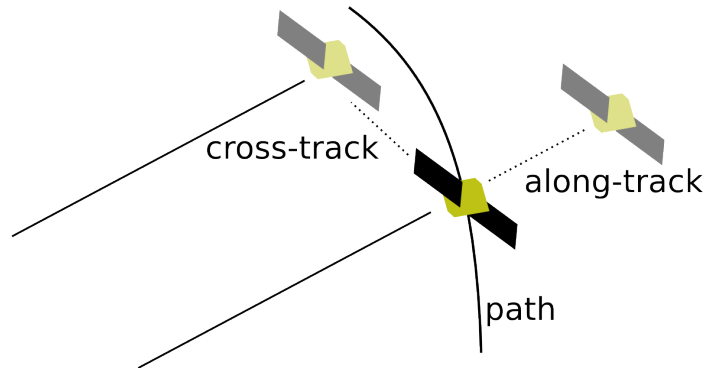


Figure 3.1: GPS Ephemeris Errors

In order to compensate for these positioning errors, precise ephemerides are available post-process (typically one to a few days later, depending on accuracy desired). The National Geodetic Survey (NGS) posts sets of these orbit parameters at [2]. More complicated models are used to generate these solutions. The model described in Section 2.3.3 was chosen so its parameters would fit compactly in the navigation message. Increases in model complexity would alter this message and therefore make significant changes to the GPS signal structure.

3.1.2 Satellite Clock Errors

The satellites in the GPS use highly stable atomic clocks so the assumption of synchronized signal transmission can be used. However, there are errors in the satellite clocks due to drift. Most of these errors can be compensated for by using a clock error model. In the navigation message, there is a clock model to use that is also estimated by the control segment, described in Section 2.3.3. The error from satellite clock drift is also on the order of 1.5 m [25]. This error is reduced from that found in Table 3.1 due to increases in control

segment capabilities and the use of more stable atomic clocks in more recent GPS satellite blocks [21].

3.2 Atmospheric Errors

As the GPS signals travel through the Earth's atmosphere, they are subject to various changes in speed. The majority of these delays come from two layers of the atmosphere: the ionosphere and troposphere. Due to the variation in composition in these layers, the amount and means of the effect are different. The various layers of the atmosphere are shown in Figure 3.2, from [3]. Since these effects are caused by the satellite signal passing through a certain portion of the atmosphere, these errors are highly correlated with respect to location. That is, if two users are in close proximity (usually taken to be in the kilometer range), the atmospheric errors on a particular satellite signal are approximately equal. The farther apart two receivers are, the less correlation between the atmospheric errors.

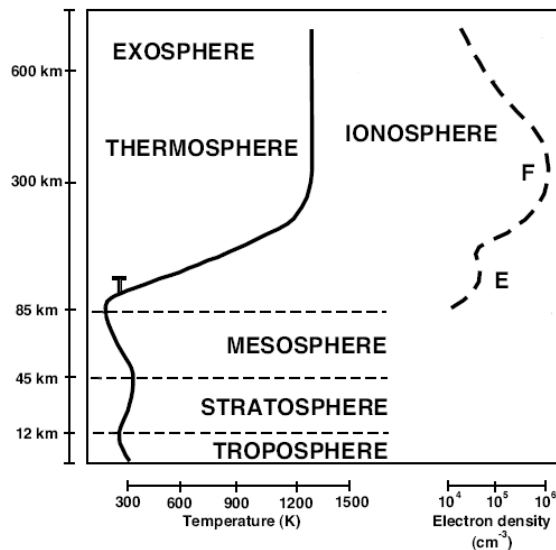


Figure 3.2: Atmospheric Layers [3]

3.2.1 Ionospheric Errors

As seen from Figure 3.2, the ionosphere is a portion of the Earth's atmosphere extending from around 85 km to over 600 km above the Earth's surface. It is characterized by ionized particles due to excitation by the Sun's ultraviolet radiation [27]. The magnitude of the effects the ionosphere has on the GPS signals is a function of the total electron content, which can change quickly as time progresses. This effect is dispersive, meaning its effect on the signal is a function of the signal frequency. This fact led, at least in part, to the use of multiple frequencies on the GPS satellites. By using measurements on multiple frequencies, the ionospheric error can be estimated and subsequently removed [6]. However, this approach requires the use of dual frequency measurements. These measurements are not often available on low-cost GPS receivers. This is due to the fact that the code on the L2 frequency is encrypted for use by authorized users only, such as the military. However, all new satellites transmit a civilian code on the L2 frequency commonly called L2C [35]. Once older satellites are phased out and replaced with updated ones, the ionosphere correction will be available to all users.

Another effect the ionosphere has on the satellite signal is that it affects the code and carrier signals differently. The dispersive media in the ionosphere delays the code, called group delay, while advancing the carrier phase, called phase advance. These two effects are equal in magnitude but opposite in sign [25]. This arises due to the fact that dispersive media make signals of different frequencies travel at different rates through the media. Since the code and carrier are signals of significantly different frequencies, their speeds are altered. For a satellite s , once the L1 ionospheric delay (I_{s1}) has been calculated, the L2 delay (I_{s2})

is also found by

$$I_{s2} = \alpha I_{s1} \quad (3.1)$$

$$\alpha = \left(\frac{f_{L1}}{f_{L2}} \right)^2 \quad (3.2)$$

Included in the satellite's broadcast navigation message are parameters for an ionospheric delay model called the Klobuchar model, shown in Equation (3.3). This model gives the L1 zenith ionospheric delay, $\hat{I}_{z,L1}$, as a function of local time, t , as

$$\frac{\hat{I}_{z,L1}}{c} = \begin{cases} A_1 + A_2 \cos\left(\frac{2\pi(t-A_3)}{A_4}\right) & |t - A_3| < \frac{A_4}{4} \\ A_1 & \text{otherwise} \end{cases} \quad (3.3)$$

where A_1 is the nighttime value of the zenith delay (fixed at 5×10^{-9} s), A_2 is the amplitude for the daytime values, A_3 is the phase peak time (fixed at 14 hours, local time), and A_4 is the period of the cosine function. Using some typical values of these parameters ($A_2 = 7$ m, $A_4 = 28$ hours) yields corrections shown in Figure 3.3 [25]. Since the ionospheric effect is a function of the amount of ultraviolet rays absorbed by the atmosphere, the model has to compensate more during the middle of the day when the Sun is directly overhead. An obliquity factor, O_F , is used to scale the zenith delay, $\hat{I}_{z,L1}$, as a function of the elevation angle to the satellite, el , as

$$O_F(el) = 1.0 + 16.0 \times (0.53 - el)^3 \quad (3.4)$$

This factor is needed since the amount of atmosphere the signal travels through is a function of the elevation angle from the horizon. At low elevation (near the horizon), the signal travels

through more of the atmosphere. Thus, the ionospheric delay is more and the model must be scaled. A plot of the obliquity factor is shown in Figure 3.4 [25].

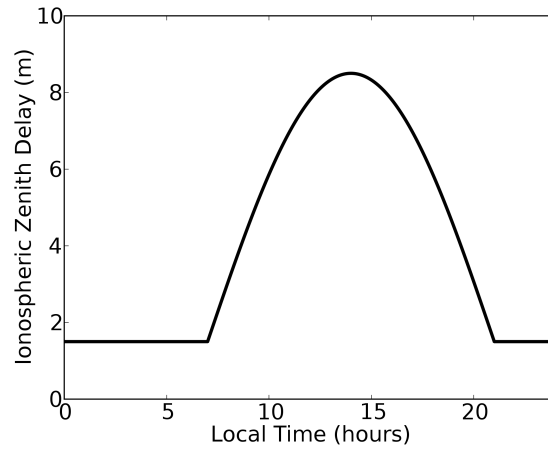


Figure 3.3: Typical Klobuchar Ionosphere Model [25]

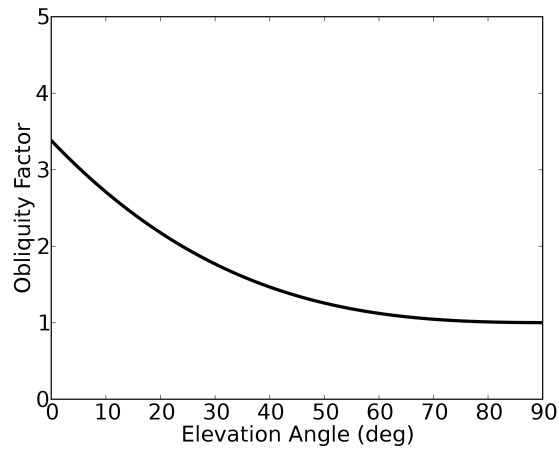


Figure 3.4: Ionospheric Obliquity Factor Model [25]

3.2.2 Tropospheric Errors

The troposphere also causes a delay in the signals passing through the atmosphere. Unlike the ionosphere, however, the delay is not a function of the frequency, so dual frequency measurements can not be used to compensate for the tropospheric error. This error mode is often broken into wet and dry components to be modeled. The wet model is dependent on the amount of moisture in the air and is therefore highly variable. However, it makes up only approximately 10% of the tropospheric error when compared to the delaying nature of the dry component. In order to compensate for this error (which is often neglected compared to other errors), a model is required [25].

3.3 Local Errors

Local errors are those that affect users on an individual basis. While the other error groupings are correlated between users, these local effects are either very weakly correlated (in the case of multipath) or uncorrelated (with regards to receiver measurement errors). Often these errors are best dealt with in receiver and antenna design as well as the user choosing a good location for the antenna. In the shadowed environments, it is the local errors that change drastically and are analyzed in this research.

3.3.1 Multipath Error

Multipath error occurs when the signal broadcast by the satellites bounces off surfaces before reaching the receiver antenna. This has a twofold effect on the signal. It first delays the signal since it takes a longer path to the receiver antenna than the line-of-sight signal. It also attenuates the signal since some of the energy is reflected in directions away from

the receiver. Research on this error source has increased in the last decade due to the effectiveness of mitigating other error sources such as the ionospheric delay, satellite errors, and the removal of Selective Availability (SA). Due to these advances, one of the next major sources of error comes from multipath [4].

Due to the fact that multipath is by nature highly dependent on the receiver antenna's immediate surroundings, it cannot be removed by differential GPS processing methods [9]. Multipath has been broken down into three different categories, each resulting from a different type of impact from surrounding objects and each having different effects on the receiver [26]. The first is specular reflection which arises from reflection off of a smooth surface. Due to the reflection, the amplitude of the signal is reduced, and the path from satellite antenna to user antenna is longer. This results in a waveform that is both lower in amplitude and out of phase with the line-of-sight signal [12]. This category greatly affects the carrier phase and is thus the major multipath effect in precise applications. The second multipath category is diffraction. This effect appears due to reflections around edges and corners of objects in the path of the signal. Lastly, when a signal bounces off a rough surface, many specular reflections occur. This is referred to as diffuse multipath. These three types of multipath are illustrated in Figure 3.5. The effects of multipath will be described more in Section 4.1. It is also noted that the multipath effect on the carrier phase measurement is much less than that on the pseudorange measurement. This will be used as a simplifying assumption in Section 4.1.

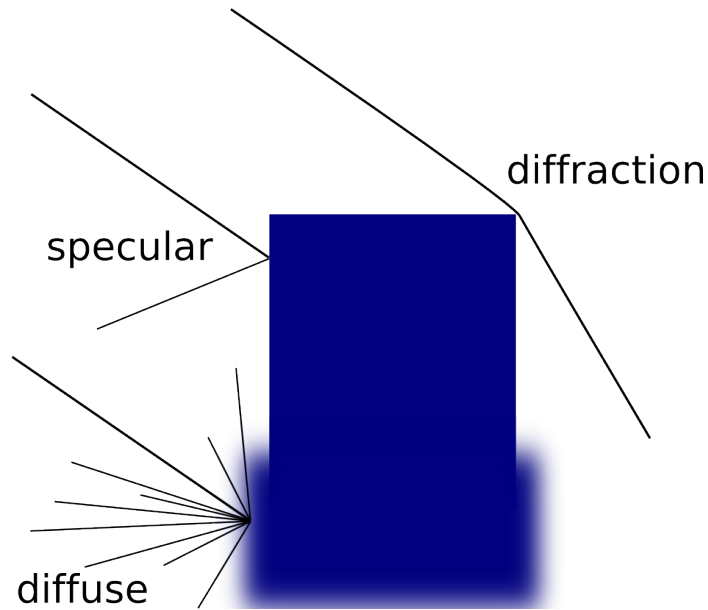


Figure 3.5: Three Multipath Types

3.3.2 Receiver Measurement Error

Several errors arise when a GPS receiver generates a measurement and brings the information it is receiving from the satellites into the discrete domain for processing. Receivers are subject to thermal noise in which the receiver tracking loops are attempting to drive an error signal to zero. This error signal is the difference between the incoming signal and the local replica of the signal. As the noise on the measurement increases, as is the case with a temperature increase, the uncertainty in the measurements is increased. Also, discretization of the signal and its subsequent processing leads to greater error. However, as advances are made in computing capabilities, these issues become less and less severe.

3.4 GPS Observable Error Models

Each of these error modes can be treated as a delay in the signal that corresponds to an additive factor in the pseudorange and carrier phase observable models. Therefore, for satellite s and L-band frequency l where $l = L1, L2$, the GPS observable models are extended from Equation (2.3) to include the errors described in this chapter as

$$\rho_{sl} = r_{bs} + c(\delta t_u + \delta t_s) + I_{sl} + T_s + M\rho_{sl} + \epsilon_{sl} \quad (3.5)$$

$$\phi_{sl} = r_{bs} + c(\delta t_u + \delta t_s) + N_{sl}\lambda_l - I_{sl} + T_s + M\phi_{sl} + \eta_{sl} \quad (3.6)$$

where $c\delta t_s$ is the satellite clock error, I_{sl} is the ionospheric error, T_s is the tropospheric error, $M\rho_{sl}$ is the pseudorange multipath error, $M\phi_{sl}$ is the carrier phase multipath error, N_{sl} is the carrier phase integer ambiguity, λ_l is the wavelength for frequency l , and η_{sl} contains the other errors on the carrier phase measurement.

3.5 Summary

This chapter has discussed the basic common errors experienced by all users of GPS receivers. As was mentioned, the three error groupings (satellite, atmospheric, and local) also roughly correspond to the amount of correlation in these errors between users. It is the local errors that are significantly affected by the surrounding environment, and it is these that are of concern in this thesis and will be analyzed in Chapter 4.

CHAPTER 4

SHADOWED ENVIRONMENTS

Shadowed environments such as heavy foliage are distinct in the errors affecting GPS operation. Although all users of GPS suffer from error modes mentioned in Chapter 3, the presence of a large number of trees also causes changes in these modes that must be considered for a user to operate under these conditions. This and other environments like urban canyons create signal blockages where a receiver is unable to track a satellite due to an obstacle blocking satellite visibility. While this adversely affects performance, there are cases when a signal is degraded so much its presence in the solution increases the error more than if it were not included at all. These environments are subject to some sort of signal blockage that degrades receiver performance but does not cause the receiver to lose lock on the signal. This degradation comes from quickly changing multipath due to a large number of objects in close proximity as well as signal attenuation due to interfering objects, shown in Figure 4.1. These are the main effects considered in this research.

4.1 Environmental Error Monitoring Parameters

In order to study how these error sources occur in heavy foliage environments, the effects considered must be determined among the general errors occurring in the GPS measurements. While monitoring the pseudorange and pseudorange rate errors is ideal, the true calculation of these metrics requires the use of a highly accurate truth system. Therefore, alternative monitoring methods were investigated. To determine signal attenuation effects

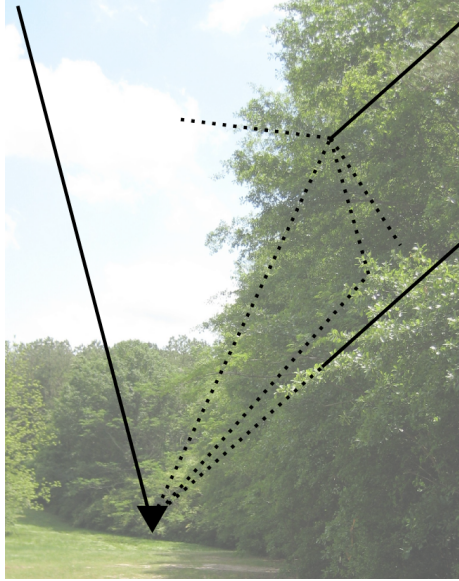


Figure 4.1: Illustration of GPS Signal Shadowing Due to Foliage

the carrier to noise ratio (C/N_0) is monitored. This gives information as to when a signal is degraded but loss-of-lock has not occurred. To monitor multipath, observation of a parameter $M1$ has been shown to be related to a receiver's pseudorange multipath [29].

4.1.1 Signal Attenuation Monitoring Parameter

Signal attenuation arises when the signal passes through foliage cover. These obstacles cause both a delay and a reduced signal amplitude which increases the difficulty of tracking the signal. This reduced amplitude effect can be seen in the C/N_0 that is reported by the GPS receiver. Decreases in the C/N_0 increase the receiver's delay-locked-loop uncertainty, σ_{tDLL} , shown in Equation (2.51). The pseudorange variance, σ_ρ^2 , is the combination of the tracking error and the atmospheric errors shown in Equation (2.50). Similarly the C/N_0 also shows the increase in the pseudorange rate variance. The pseudorange rate is related

to the receiver's measurement of the Doppler frequency as

$$\dot{\rho}_s = -\frac{c}{f_{L1}} f_{D,s} \quad (4.1)$$

The variance of the Doppler frequency is related to the noise on the Frequency-Lock-Loop (FLL) that tracks the frequency of the incoming signal. The thermal variance of the FLL is therefore taken to be [36]

$$\sigma_{tFLL} = \frac{\lambda_L}{2\pi T} \sqrt{\frac{4FB_n}{C/N_0} \left[1 + \frac{1}{TC/N_0} \right]} \quad (4.2)$$

Again the values of the parameters in Equation 4.2 are assumed from typical values found in [36] and shown in Table 4.1.

Table 4.1: Frequency-Lock-Loop Parameters from [36]

Parameter	Description	Value	Units
F	loop factor	1	-
B_n	frequency loop noise bandwidth	2	Hz
T	predetection integration time	2	ms
λ_L	carrier wavelength	0.19	m

However, the FLL (and therefore the pseudorange rate measurement) is also a function of the dynamic stress error on the tracking loop, f_e . These stresses are due to the dynamics of the receiver antenna. Assuming mild dynamics with a dynamic stress of $f_e = 3\text{Hz}$ and taking the FLL variance to be the pseudorange rate variance, i.e. $\sigma_{\dot{\rho}}^2 = \sigma_{FLL}^2$, the pseudorange rate variance is therefore [36]

$$\sigma_{\dot{\rho}}^2 = \left(\sigma_{tFLL} + \frac{f_e}{3} \right)^2 \quad (4.3)$$

Since the variances on the pseudorange and pseudorange rate are both functions of the C/N_0 , this parameter is chosen for monitoring the errors in shadowed environments.

4.1.2 Multipath Monitoring Parameter

The other dominant effect to monitor is the changing multipath. As was discussed in Section 3.3.1, objects near the GPS antenna can alter the propagated signal by reflection. Depending on the local surroundings, these objects may reflect toward the antenna multiple delayed copies of the same signal. A receiver attempts to track the combination of all copies of the signal, which leads to decreased performance. Since the reflected path is always longer than the direct path, the multipath signals are always delayed. The reflected signals are also typically weaker than the line-of-sight signal depending on the nature of the reflection. As seen in Figure 4.1, multipath often causes a large change in the line-of-sight to the signal source. This error mode also affects the receiver's range rate measurement since the antenna's velocity projected onto the line-of-sight vector to the satellite is different from its projection onto the reflected path.

In order to quantify these multipath effects, a multipath monitoring variable, labeled $M1$ in this thesis, is used. For a given satellite, three measurements are used to derive the $M1$ parameter: the L1 pseudorange and L1 and L2 carrier phase. These measurements are shown in their common form with the error sources being added to the true range in Equations (3.5) and (3.6). It should be noted that the multipath on the carrier phase, $M\phi_i$, is significantly less than the multipath on the pseudorange, $M\rho_i$ [29], i.e. $M\phi_i \ll M\rho_i$.

Using the carrier phase model in Equation (3.6) and the dual frequency ionosphere relation in Equation (3.1) the L1 ionosphere delay can be found as

$$\begin{aligned} \phi_1 - \phi_2 &= N_1\lambda_1 - N_2\lambda_2 - I_1 + I_2 + M\phi_1 - M\phi_2 \\ \Rightarrow \quad I_1 &= \frac{\phi_1 - \phi_2}{\alpha - 1} - \frac{N_1\lambda_1 - N_2\lambda_2}{\alpha - 1} - \frac{M\phi_1 - M\phi_2}{\alpha - 1} \end{aligned} \quad (4.4)$$

where the noise term is dropped. Since these parameters are using values from only one satellite, s is also removed from the notation. Combining Equation (4.4) with the L1 carrier phase in Equation (3.6) removes the ionosphere delay as

$$\begin{aligned} \phi_1 + \frac{\phi_1 - \phi_2}{\alpha - 1} &= r_s + c(\delta t_u + \delta t_s) + N_1\lambda_1 + \frac{N_1\lambda_1 - N_2\lambda_2}{\alpha - 1} \\ &\quad + M\phi_1 + \frac{M\phi_1 - M\phi_2}{\alpha - 1} + T_1 \end{aligned} \quad (4.5)$$

Then combining Equation (3.5) with Equations (4.4) and (4.5) gives

$$M1 = \rho_1 - \left(1 + \frac{2}{\alpha - 1}\right)\phi_1 + \left(\frac{2}{\alpha - 1}\right)\phi_2 \quad (4.6)$$

$$= -N_1\lambda_1 - 2\frac{N_1\lambda_1 - N_2\lambda_2}{\alpha - 1} + M\rho_1 - M\phi_1 - 2\frac{M\phi_1 - M\phi_2}{\alpha - 1} \quad (4.7)$$

$$\approx B_1 + M\rho_1 \quad (4.8)$$

where the carrier phase multipath variables have been neglected and the bias term

$$B_1 = -N_1\lambda_1 - 2\frac{N_1\lambda_1 - N_2\lambda_2}{\alpha - 1} \quad (4.9)$$

is a function of the integer ambiguities on the dual frequency carrier phase measurements.

This bias term, B_1 can be removed by averaging or taking the first $M1$ measurement as the bias term [29]. For this work, the change in multipath is being monitored so calculating the difference between successive $M1$ variables removes the bias term. This approximates the change in L1 pseudorange multipath which is the effect to be monitored. Since B_1 is a function of the integer ambiguities a cycle slip will change the bias. This would appear as a spike in the $M1$ variable. This effect is neglected in the analysis but is a source of additional error that could be considered in future work.

Since L1 pseudorange and L1 and L2 carrier phase measurements are required for this analysis, static dual-frequency data was collected using a NovAtel DL-V3 receiver with a NovAtel dual-frequency antenna. The photo in Figure 4.2 shows the location of the static analysis since it provided a good contrast between clear view and heavy foliage. This allowed for clear distinctions between the two environments to be drawn. A visualization technique was then used to evaluate these effects in heavy foliage.

4.1.3 Error Visualization for a Single Satellite

In order to determine the total effect of foliage cover on the satellite signals, a visualization technique for a single satellite was developed. Both monitoring variables ($M1$ and C/N_0) can be plotted together to visualize the signal error at a point in time. For a single satellite, this is shown in Figure 4.3. The change in $MP1$ is shown as the magnitude in this error plot. The C/N_0 is shown as the shade in the plot. These monitoring variables together reveal the effects of the environment on the signal. Figure 4.3 shows these monitoring variables for a single satellite signal as it passes from heavy foliage to a clear sky



Figure 4.2: Static Data Collection Location

view. This diagram shows that the signal strength drops and multipath jumps correspond with each other, although not directly.

4.1.4 Error Visualization for All Satellites in View

The single satellite visualization technique was extended to produce a visualization technique for all satellites in view. For a better view of what happens in tree cover, the static location shown in Figure 4.2 was again used. This location had heavy tree cover on the west side and clear sky on the east side. The aerial view of this area is shown in Figure 4.4. The combination of all satellite's monitoring variables are shown in Figure 4.5. This plot is similar to Figure 4.3 except that each of the $M1$ and C/N_0 plots are bent to follow the path that the satellite travels across the sky. This allows spatially correlated effects to be shown. Since there is a relatively distinct dividing line between the two regions, the distinction can

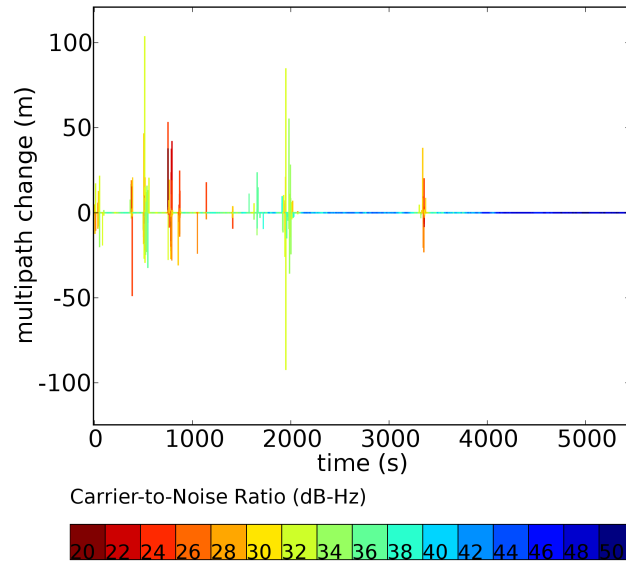


Figure 4.3: Single Satellite Error Visualization

also be seen in the sky plot of Figure 4.5. This plot shows the effect that foliage has in quickly changing the multipath as well as degrading the signal. Low-elevation effects are also shown as satellites get close to the outer circle. This plotting scheme is extended from [17] where only the actual multipath is plotted with respect to satellite azimuth and elevation. The visualization developed for this thesis shows the changing effects of the multipath as well as the signal strength for analysis in changing conditions.

4.1.5 Analysis Results

From the monitoring variable plots shown in Figures 4.3 and 4.5, the shadowing effects of heavy foliage are shown to degrade the satellite signals. Even when a signal is still being tracked and is available to the system, low signal power (shown through low C/N_0 values)



Figure 4.4: Aerial View of Static Data Location

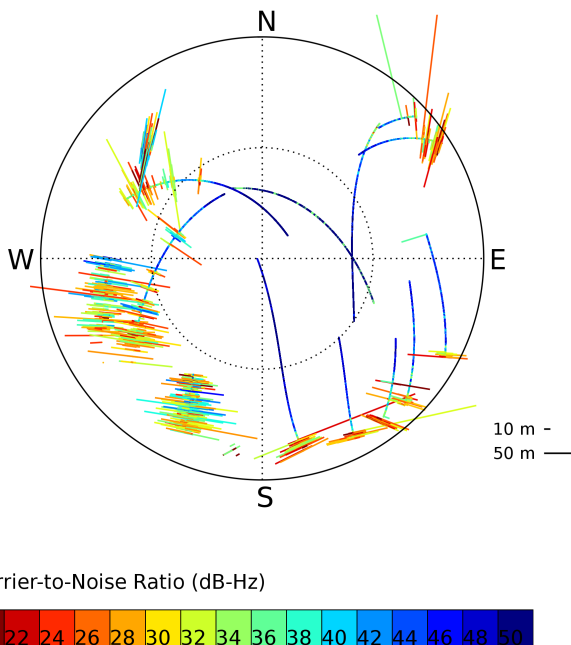


Figure 4.5: All-In-View Satellite Error Visualization

and large jumps in the multipath (seen through $M1$ variable) indicate that accuracy is degraded.

4.2 Summary

This chapter discusses the error modes specific to shadowed environments and the technique developed for their analysis. Monitoring variables were chosen to visualize the effects of foliage blocking a satellite signal. Although these effects usually cause a signal to drop out of view due to blockage, the analysis shows that even when satellites are still available, their accuracy is compromised due to the shadowing effects. This chapter motivates the need to develop a solution for operation in these environments, which is presented in Chapter 5.

CHAPTER 5

ERROR MITIGATION

The analysis presented in Chapter 4 motivates the need for methods to mitigate errors specific to shadowed environments. These errors include signal attenuation and quickly changing multipath. Both these error modes cause an increase in the uncertainty of the GPS receiver measurements and thus degraded navigation performance. Error mitigation is necessary to obtain accurate and reliable navigation solutions for operation in shadowed environments. From the design requirements in Chapter 1, the system must be low cost, operate continuously, and avoid solution spikes so it can be used in conjunction with vehicle navigation and control systems. In Chapter 4 it was shown that a stand-alone GPS receiver will not meet these requirements. Two methods of improved operation are presented here: differential corrections and sensor coupling. Although the use of differential corrections is very common and improves the accuracy of GPS solutions relative to a base receiver, the shadowing specific errors presented in Chapter 4 cause differential methods to also fail since these effects are not compensated in the correcting algorithms. Therefore the solution implemented in this thesis is integration with an inertial sensor in a closely coupled architecture with fault detection and exclusion (FDE) performed by an innovation monitoring technique [14].

5.1 Differential Corrections

GPS accuracy can be improved with the use of other local GPS receivers [28]. This is accomplished by operating on GPS measurements to calculate the position of one receiver

relative to the other. With this as the goal, there are methods that can reduce or even eliminate some of the aforementioned error types. The differential research presented here was conducted as an attempt to improve relative positioning between multiple receivers. This relative position can be used to determine an accurate global position for a mobile receiver if the base receiver is placed at a known, surveyed location.

5.1.1 Position Differencing

The most basic of differential positioning methods is to take the difference of two independently calculated positions. This method assumes the correlated range errors detailed in the pseudorange and carrier phase Equations (3.5) and (3.6) result in a correlated error in position. The differencing removes position error that is common to the two receivers. However, even though the error sources may be correlated between two receivers, their combined effects on the position solution changes the amount of correlation. This method tends to remove some errors common to both calculated positions, but the combination is not a linear differencing of the errors. This is due to the fact that the differencing is done in the position domain rather than the range domain. In this case, the individual solutions are calculated using biased and noisy measurements as described in Equations (3.5) and (3.6) to generate a solution based on methods similar to the one described in Section 2.4. These independently calculated positions can also have corrections applied using commercial or freely available corrections such as Omnistar or the Wide Area Augmentation System (WAAS), respectively. This typically reduces the global position error of each of the independent solutions to around three meters. After differencing these two corrected

positions, the relative positioning error is on the order of one meter for a commercial receiver. Note that these differences are subject to large jumps since errors can vary quickly between receivers.

5.1.2 Code Differencing

If the measurements of two receivers are temporally and spatially correlated, several of the delay errors in the range measurement can be removed if the actual measurements are differenced before the position solution is calculated. This error correlation was described previously in Chapter 3. If two receivers, A and B , can view the same satellite, j , as shown in Figure 5.1, differencing these two ranges removes the errors common between them. This is called single differencing, and it removes the common satellite clock error, δt_j .

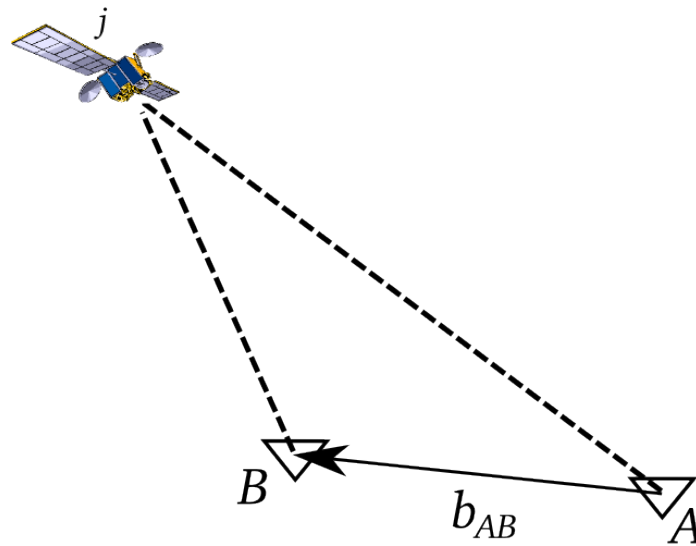


Figure 5.1: Common Satellite

The resulting single difference models are shown in Equations (5.1) and (5.2) where the L1 frequency is assumed.

$$\rho_{j,AB} = r_{AB} + c\delta t_{AB} + I_{j,AB} + T_{j,AB} + M\rho_{j,AB} + \epsilon_{s,AB} \quad (5.1)$$

$$\phi_{j,AB} = r_{AB} + c\delta t_{AB} + N_{j,AB}\lambda - I_{j,AB} + T_{j,AB} + M\phi_{j,AB} + \eta_{s,AB} \quad (5.2)$$

Note in both equations, the components A and B are combined into similar terms representing the difference in each component between the receivers for the satellite j , noted as AB . Also note the differencing of the measurements includes the noise from each measurement, thus increasing the noise of the new combined measurement. The single difference measurements can be useful when considered along with Figure 5.2. Here it is shown that the single differenced measurement is related to the baseline by the unit vector to the satellite, j .

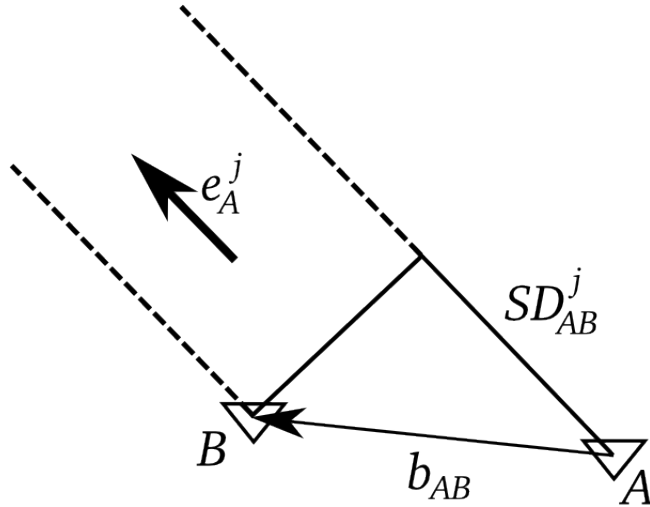


Figure 5.2: Single Difference Diagram

Assuming the distance to the satellite is much greater than the baseline length, the unit vectors from receivers A and B are approximately the same. As an example, assuming

a baseline of 10 km with the average satellite altitude of 20,200 km above the receivers A and B with the satellite directly above receiver A , the angle of separation, ζ , between the two receivers as viewed from the satellite would be $\frac{20200 \text{ km}}{\sin(\frac{\pi}{2} \text{ rad})} = \frac{10 \text{ km}}{\sin(\zeta)} \Rightarrow \zeta \simeq 0.000495 \text{ rad}$. This angle also becomes the difference in elevation angle from satellite B to the satellite and therefore the error that would be included in the direction of the unit vector.

From Figure 5.2, Equation (5.3) can be formed.

$$\begin{aligned} SD_{j,AB} &= u_{jA} \cdot b_{AB} \\ &= |u_{jA}| |b_{AB}| \cos(\theta) \end{aligned} \tag{5.3}$$

Where θ is the angle between the unit vector to the satellite, u_{jA} and the baseline vector, b_{AB} . Since this angle is assumed to be $\frac{\pi}{2}$ rad with an error of ζ at the point of consideration, the equation expands to

$$\begin{aligned} SD_{j,AB} &= |e_A^j| |b_{AB}| \cos(\theta - \zeta) \\ &= 10 \text{ km} \sin(\zeta) \\ &\simeq 1.225 \text{ mm} \end{aligned}$$

Therefore, even under these poor conditions, the error is insignificant compared to the noise on the single difference measurement. Also note if the receivers are spatially correlated, their atmospheric errors are approximately equal, thus $I_{j,AB} \simeq T_{j,AB} \simeq 0$.

Using two single differences for satellites j and k , these two measurements can be combined to form double differences, shown in Equations (5.4) and (5.5) and illustrated in

Figure 5.3

$$\rho_{jk,AB} = r_{jk,AB} + \epsilon_{jk,AB} \quad (5.4)$$

$$\phi_{jk,AB} = r_{jk,AB} + N_{jk,AB}\lambda + \eta_{jk,AB} \quad (5.5)$$

This differencing removes the user clock bias, δt_{AB} , which was common to both single

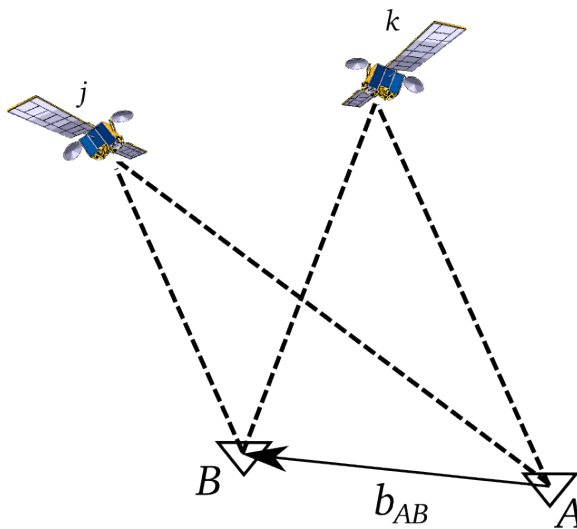


Figure 5.3: Two Common Satellites

differences. This removes the requirement that the clock bias must be estimated. However, this comes at the expense of further increasing the noise on these new quantities. Also notice that the integer ambiguities in the carrier phases ($N_{j,A}$, $N_{j,B}$, $N_{k,A}$, and $N_{k,B}$) are lumped into a single ambiguity ($N_{jk,AB}$) that must be estimated rather than the four integer ambiguities in the original measurements shown in Equation(3.6). Similar to the single difference, the double difference can be related to the baseline as

$$DD_{jk,AB} = (u_{jA} - u_{kA}) \cdot b_{AB} \quad (5.6)$$

Placing all available double differences with each differenced about satellite j 's single difference into matrix form yields a relation to estimate the baseline in Equation (5.7)

$$\begin{bmatrix} u_{jA} - u_{kA} \\ \vdots \\ u_{jA} - u_{mA} \end{bmatrix} \cdot b_{AB} = \begin{bmatrix} DD_{jk,AB} \\ \vdots \\ DD_{jm,AB} \end{bmatrix} \quad (5.7)$$

5.1.3 Carrier Smoothed Code Differencing

The methods described so far do not make use of the highly accurate carrier phase measurement due to the difficulty of estimating the double difference integer ambiguities, $N_{jk,AB}$. However, these ambiguities are constant over time, assuming no cycle slips have occurred. A smoothing method is used in which a double difference range, DD , is estimated using the carrier phase double difference ($\phi_{jk,AB}$) and the pseudorange double difference ($\rho_{jk,AB}$). By using the carrier phase double differences at two time epochs ($\phi_{jk,AB}^n$ and $\phi_{jk,AB}^{n-1}$) to determine the change in the double difference range (DD), a low noise measurement is obtained of the change in the double difference over one time step. By combining these measurements in a Kalman filter, the double difference range (DD) can be calculated which uses the low noise carrier phase double differences ($\phi_{jk,AB}$) to remove the noise inherent in the code double difference ($\rho_{jk,AB}$). The resulting measurement is a very smooth double difference that lies along the mean of the code double difference measurement. To calculate the smoothed difference, Equations (5.8) through (5.12) are employed.

$$DD^- = DD^+ + \lambda \left(\phi_{jk,AB}^n - \phi_{jk,AB}^{n-1} \right) \quad (5.8)$$

$$P = P + Q \quad (5.9)$$

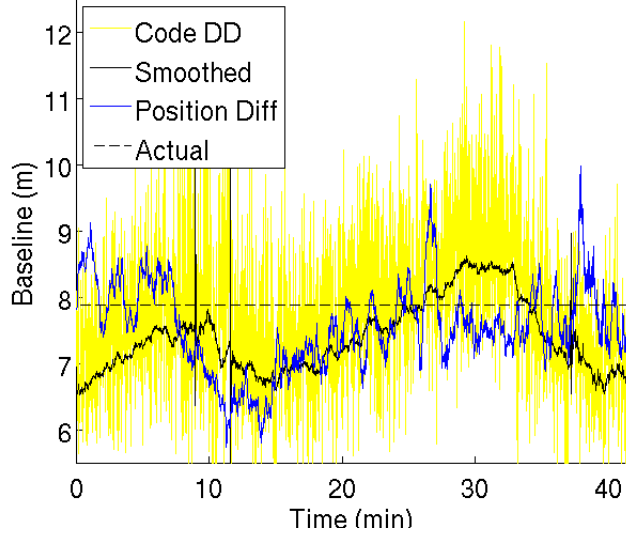


Figure 5.4: Method Comparison

$$K = P(P + R)^{-1} \quad (5.10)$$

$$DD^+ = DD^- + K(DD^- + \rho_{jk,AB}^n) \quad (5.11)$$

$$P = (I - K)P \quad (5.12)$$

Here P is the properly initialized covariance matrix, Q is the process noise covariance, R is the measurement covariance, and K is the resulting Kalman gain.

5.1.4 Static Comparison of Differential Methods

The three differential methods are shown in Figure 5.4 for a static case. In this comparison the code double difference performed the worst with a 3D standard deviation of 1.2 m. The carrier smoothed and position difference estimates were fairly close to the same performance with deviations of 0.54 m and 0.67 m, respectively.

The noise performance of the smoothed double difference is slightly better than that of the raw position differencing due to the low noise of the carrier phase measurements. However, both suffer from drift about the true relative position magnitude (baseline). This drift results in errors of approximately one meter from the actual baseline. Assuming a well surveyed base position, the global position will be accurate to about one meter. This is an improvement over the global accuracy of a single receiver. However, the double difference processing techniques do not provide a significant advantage over the raw position differencing. Another difficulty in applying these methods to roving vehicles is the requirement for a surveyed base station and data link between the receivers. Also, as the baseline grows, the differential methods suffer a drop in performance. This is due to the fact that the error correlation decreases and each receiver may be tracking different satellites. Therefore an onboard solution is desired and described in this thesis.

5.2 Inertial Aiding Sensors

An alternative to coupling multiple GPS receivers is to use alternative sensors, particularly an inertial measurement unit (IMU). Since inertial sensors have high output rates and low short-term noise, they are well suited for navigation and control over short periods of time. The length of this time is dependent on the grade of IMU used [37] since these sensors tend to drift over time. To keep the system low-cost, an automotive grade IMU, the Xbow 440, was used. The long-term stability and bounded nature of the GPS navigation solution tends to make it a perfect sensor to couple with an IMU in a way that takes advantage of the strengths of both systems while reducing the effects of their weaknesses [14].

5.2.1 Coupling Architectures

For this system, three coupling architectures found in the literature were considered [15]. These are shown in Figure 5.5. The IMU mechanization equations propagated the desired states. For general operation, a six degree of freedom order was chosen to include three body axes of both linear and rotational motion. The differences in the considered architectures stems from which measurements are used by the coupling filter and whether or not the GPS receiver is aided by the filter. In a loosely coupled approach, the receiver calculates a solution using at least four satellites, and its position and velocity are used as measurements. This solution is independent of the coupling solution. One major disadvantage of this method is that when the receiver cannot track enough satellites to compute the independent position, velocity, and time (PVT) solution, no GPS aiding measurements are available. Therefore the coupled solution accuracy is determined by the drift characteristics of the low-cost IMU. In the closely coupled architecture, pseudorange and pseudorange rate are used as measurements from any available satellite measurement. Therefore the updating is continued with less than 4 satellites. In this case, the GPS position calculation is moved into the coupling filter rather than being performed independently. Finally, a tightly coupled system also uses pseudorange and pseudorange rate measurements, but the IMU is used to aid the receiver in tracking GPS satellite signals. This approach increases the capabilities of tracking in GPS harsh environments, particularly dynamic maneuvers. However, it requires the use of a GPS receiver that can accept the aiding measurements. The nomenclature for these methods has changed over time but these labels effectively delineate the architecture being used. For this work, closely coupled integration is chosen since it

continuously updates errors but does not require GPS hardware to make use of the IMU aiding information.

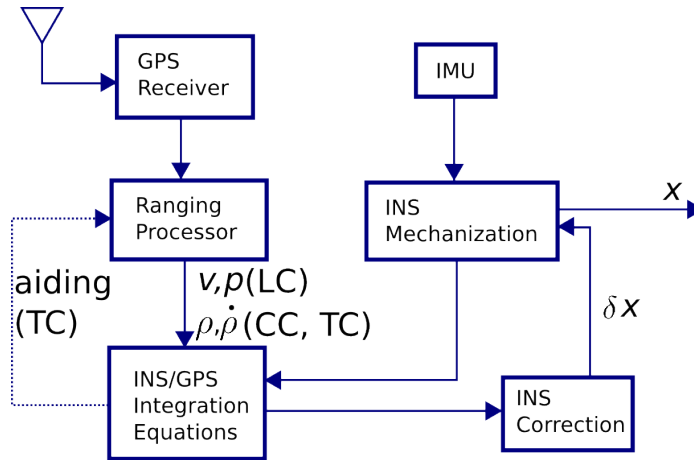


Figure 5.5: Coupling Architectures

5.2.2 INS Mechanization Equations

Since the coupling algorithm corrects solutions generated by the IMU, a navigation solution is given by these corrected measurements from the IMU mechanization equations. The IMU combined with its mechanization is called an inertial navigation system (INS). This system includes the raw IMU measurements and the technique used to convert these measures into navigation states. The IMU measurements of angular rates, $\omega_{ib}^b = [g_x \ g_y \ g_z]^T$, and specific force, $f_{ib}^b = [f_x \ f_y \ f_z]^T$, are used to drive these states as shown in Equations (5.14 - 5.17). To simplify notation, Ω_{ib}^b is the skew-symmetric form of the angular rate

vector ω_{ib}^b such that

$$\Omega_{ib}^b = \begin{bmatrix} 0 & -g_z & g_y \\ g_z & 0 & -g_x \\ -g_y & g_x & 0 \end{bmatrix} \quad (5.13)$$

Taking Δt as the IMU measurement time step, the coordinate transformation matrix, C_b^e , from the body frame, b , to the ECEF frame, e , is propagated as [14]

$$C_b^e = C_b^e \cdot (I_3 + \Omega_{ib}^b \Delta t) - (\Omega_{ie}^e \cdot C_b^e) \Delta t \quad (5.14)$$

The specific force vector is translated to the ECEF frame by

$$f_{ib}^e = C_b^e \cdot f_{ib}^b \quad (5.15)$$

With the acceleration due to gravity and earth rotation given as g_b^e , the velocity state is propagated as

$$v_{eb}^e = v_{eb}^e + (f_{ib}^e + g_b^e - 2\Omega_{ie}^e \cdot v_{eb}^e) \Delta t \quad (5.16)$$

The position vector can then be updated as

$$r_{eb}^e = r_{eb}^e + v_{eb}^e \Delta t \quad (5.17)$$

Simple Euler numerical integration schemes were chosen for ease of computation. Although the error due to this numerical approximation would tend to accumulate over long time periods, with GPS corrections this effect is reduced.

Equations (5.14 - 5.17) are processed whenever a new measurement is available from the IMU. As correction measurements (GPS observables) are available, the position (r_{eb}^e), velocity (v_{eb}^e), and coordinate transformation matrix (C_b^e) are updated to include these corrections. This correction process is detailed in subsequent sections. By periodically applying the corrections, the INS solution represents the system's best estimate of the antenna's navigation state at the current time. In the implementation described in Sections 5.2.4 and 5.2.5, this INS solution is used to linearized the state and measurement equations.

5.2.3 State Vector

The GPS/INS integration scheme includes 17 states used to keep track of the vehicle's motion, shown in Equation (5.18).

$$x = \begin{bmatrix} \delta\psi_{eb}^e \\ \delta v_{eb}^e \\ \delta r_{eb}^e \\ b_a \\ b_g \\ cdt_u \\ c\dot{d}t_u \end{bmatrix} \quad (5.18)$$

These states are partitioned into six groupings of similar variables. The state vector includes three components of attitude error, ψ_{eb}^e , which are used to update the coordinate

transformation matrix from body to ECEF frames, C_b^e ; three components of velocity error in the ECEF frame, v_{eb}^e ; and three components of position error in the ECEF frame, r_{eb}^e . The three accelerometer biases, b_a , and three gyro biases, b_g , are included and modeled as constants with process noise. The receiver clock bias, cdt_u , and drift, \dot{cdt}_u , are included with the clock drift modeled as a constant.

5.2.4 State Dynamics

Since the INS provides a set of nonlinear dynamic equations to propagate the state vector in Equation (5.18) and the GPS measurements are nonlinear functions of these states (to be described in Section 5.2.5), an Extended Kalman Filter (EKF) can be used in the integration scheme [14]. In order to use the coupling architecture in an EKF form, the equations given in Section 5.2.2 are linearized for propagation of the state errors (δx) and its error covariance matrix (P). The state vector includes errors of the attitude, velocity, and position states but keeps track of the actual IMU bias and receiver clock states rather than their errors. The form of the state equation is

$$\dot{\delta x} = F\delta x + w_s \tag{5.19}$$

where

$$F = \begin{bmatrix} -\Omega_{ie}^e & O_3 & O_3 & O_3 & C_b^e & O_2 \\ F_{21} & -2\Omega_{ie}^e & F_{23} & C_b^e & O_3 & O_2 \\ O_3 & I_3 & O_3 & O_3 & O_3 & O_2 \\ O_3 & O_3 & O_3 & O_3 & O_3 & O_2 \\ O_3 & O_3 & O_3 & O_3 & O_3 & O_2 \\ O_2^T & O_2^T & O_2^T & O_2^T & O_2^T & F_{66} \end{bmatrix} \quad (5.20)$$

$$F_{21} = \begin{bmatrix} 0 & -f_z & f_y \\ f_z & 0 & -f_x \\ -f_y & f_x & 0 \end{bmatrix} \quad (5.21)$$

$$F_{23} = \frac{2g_0}{r_{en}^e} \frac{r_{eb}^e r_{eb}^{eT}}{|r_{eb}^e|} \quad (5.22)$$

$$F_{66} = \begin{bmatrix} 0 & 1 \\ 0 & 0 \end{bmatrix} \quad (5.23)$$

where I_m represents an identity matrix of size $m \times m$, O_3 represents a 3×3 null matrix, O_2 is a 3×2 null matrix, and w_s is the process noise included in the system derivation.

The state transition matrix at the current time step, k , can be approximated as

$$\Phi_k = I_{17} + F\Delta t \quad (5.24)$$

This allows for the propagation of the state correction as

$$\delta x_k^- = \Phi_k \delta x_{k-1}^+ \quad (5.25)$$

With the state transition matrix, the covariance matrix can be updated to

$$P_k^- = \Phi_k P_{k-1}^+ \Phi_k^T + Q \quad (5.26)$$

Here Q is the system noise covariance matrix which is assumed to be a diagonal matrix with entries given in Table 5.1. These values were tuned by trial and error to achieve the desired performance.

Table 5.1: System Noise Covariance Matrix Values

State	Value	Units
Attitude Errors	0.01	(rad/s) ²
Velocity Errors	0.01	(m/s) ²
Position Errors	0.0005	(m) ²
Accelerometer Bias Errors	0.000001	(m/s ²) ²
Gyro Bias Errors	0.000001	(rad/s) ²
Clock Bias Error	0.1	(m) ²
Clock Drift Error	0.01	(m/s) ²

5.2.5 State Measurement Relations

The GPS/INS integration scheme uses measurements from all available satellites to update the state corrections as

$$z = H\delta x + w_m \quad (5.27)$$

where H is the state-measurement matrix and w_m is the measurement error included for derivation.

For satellite s , pseudorange, ρ_s , and pseudorange rate, $\dot{\rho}_s$, measurements are provided by the receiver. The rate measurement comes from the receiver's Doppler frequency measurement, f_{Ds} . This measure is transformed to a rate measurement as

$$\dot{\rho}_s = -\frac{c}{f_{L1}} f_{Ds} \quad (5.28)$$

where c is the speed of light and f_{L1} is the L1 carrier frequency. For each satellite, s , these quantities (ρ_s and $\dot{\rho}_s$) make up the measurements available to the navigation system at each measurement update.

Estimates of these measurements are calculated from the corrected INS solution, which is the system's best estimate of the state just before the measurement, and the GPS position and velocity described in Sections 2.3.3 and 2.3.3. These estimated pseudorange and pseudorange rate measurements are calculated as

$$\hat{\rho}_s = \sqrt{(r_{eb}^e - r_{es}^e)^T \cdot (r_{eb}^e - r_{es}^e)} + cdt_u \quad (5.29)$$

$$\hat{\dot{\rho}}_s = \frac{(r_{eb}^e - r_{es}^e)^T \cdot (v_{eb}^e - v_{es}^e)}{\sqrt{(r_{eb}^e - r_{es}^e)^T \cdot (r_{eb}^e - r_{es}^e)}} + c\dot{d}t_u \quad (5.30)$$

The differences in the measurements (ρ_s and $\dot{\rho}_s$) and estimated measurements ($\hat{\rho}_s$ and $\hat{\dot{\rho}}_s$) give the measurement innovations. These differences are used both to correct the state estimates and to run the fault detection and exclusion algorithm, described in Section 5.3. These innovations are calculated as

$$\delta z_{\rho_s} = \rho_s - \hat{\rho}_s \quad (5.31)$$

$$\delta z_{\dot{\rho}_s} = \dot{\rho}_s - \hat{\dot{\rho}}_s \quad (5.32)$$

The innovations represent the new information provided to the navigation EKF. If the estimated measurement is close to the actual measurement, the innovation corresponding to this measurement will be low. In this case, the portion of the navigation filter corresponding to this innovation will have little effect on altering the state correction (δx). Alternatively if the estimated state has drifted significantly, the estimated and actual measurements will diverge and the corresponding innovation will be relatively large. Thus the navigation filter will tend to alter the state correction to drive the innovation closer to zero.

Placing all of the innovations in a column vector forms the measurement vector as

$$z = \begin{bmatrix} \delta z_{\rho_1} \\ \vdots \\ \delta z_{\rho_1} \\ \vdots \end{bmatrix} \quad (5.33)$$

The integration equations use a standard Extended Kalman Filter algorithm with the states described in Equation (5.18). The system is placed in linear form by differentiating the estimated measurements in Equations (5.29) and (5.30) with respect to each of the states. Approximations for this measurement state relationship matrix are made in [14] and are used here. For each row corresponding to a pseudorange, the resulting H matrix entry is

$$H_{\rho_s} = [O_3 \quad O_3 \quad u_{su} \quad O_3 \quad O_3 \quad 1 \quad 0] \quad (5.34)$$

where u_{su} is the unit vector from the satellite s to the user. Similarly, for each row corresponding to a pseudorange rate, the resulting H matrix entry is

$$H_{\dot{\rho}_s} = [O_3 \quad u_{su} \quad O_3 \quad O_3 \quad O_3 \quad 0 \quad 1] \quad (5.35)$$

Assuming uncorrelated measurements, the variances of these measurements are used as entries along the diagonal of the measurement covariance matrix, R . The variance for a pseudorange measurement is described in Equation (2.50). The variance for a pseudorange rate measurement is assumed to be a function of the frequency-lock-loop (FLL) that generates the Doppler frequency measurement used in Equation (5.28). It is therefore taken from values given in [21] where the FLL thermal variance is taken to be

$$\sigma_{tFLL} = \frac{\lambda_L}{2\pi T} \sqrt{\frac{4FB_n}{C/N_0} \left[1 + \frac{1}{TC/N_0} \right]} \quad (5.36)$$

with parameters defined by the tracking loop architecture, shown in Table 4.1. The Doppler frequency variance is then

$$\sigma_{\dot{\rho}} = \sqrt{\sigma_{tFLL}^2 + \frac{f_e^2}{9}} \quad (5.37)$$

where f_e is the dynamic stress error, taken to be 3 m/s. At a given time step, if a set of measurements are available, the measurement innovation vector, z , is generated and the Kalman gain calculated as

$$K = P_k^- H^T \left(H P_k^- H^T + R \right)^{-1} \quad (5.38)$$

where the measurement covariance matrix (R) is a diagonal matrix with elements corresponding to the pseudorange and pseudorange rate variances, described in Equations (2.50) and (5.36), respectively. Both of these variances for each satellite signal are functions of the signal's C/N_0 , which represents the strength of the signal at the antenna. Lastly, the state error and covariance matrix are updated using the measurements.

$$\delta x_k^+ = \delta x_k^- + Kz \quad (5.39)$$

$$P_k^+ = (I_{17} - KH) P_k^- \quad (5.40)$$

5.3 Fault Detection and Exclusion

Fault detection refers to the ability of a system to determine if there is a significant degradation in the GPS solution. The user is alerted if the system cannot guarantee solution accuracy to a certain level [14]. Fault exclusion provides a means to remove the fault and continue operation with the desired accuracy without having to alert the user. These schemes are used for critical applications where GPS availability and accuracy are necessary, such as aircraft landings. Traditionally these methods are used to detect and correct satellite failures. In this thesis, the errors being studied cause sporadic measurement outliers due to tree cover. These outliers are caused by large instantaneous jumps in multipath and corresponding drops in the signal power at the antenna. They are considered outliers since these measurements contain errors that cause the range or range rate to be outside the expected accuracy of the GPS observables. Therefore a technique is used to exclude outlying measurements and provide a more robust solution.

5.3.1 Normalized Innovation Parameter

Since the errors in multipath and signal attenuation affect the receiver measurements and these errors enter the solution through the innovation (described in Section 5.2.5), the innovation was chosen as the detection parameter. However, since the innovation is a function of measurement noise and not just these errors, jumps might not necessarily imply a fault. Therefore a normalization routine was implemented to provide more consistent operation. Each innovation is normalized by the square root of the C matrix diagonal, where $C = HPH^T + R$. The C matrix is calculated as part of Equation (5.38) and therefore does not greatly increase the computational burden. Thus, the normalized innovation is

$$y_i = \frac{z_i}{\sqrt{C_{ii}}} \quad (5.41)$$

5.3.2 FDE Threshold

The normalized innovation parameters in Equation (5.41) are compared to a previously determined threshold, y_t . The measurement and its corresponding rows in the H and R matrix are removed if it is faulty, i.e. $y_i > y_t$. The threshold value is determined using the assumption that the normalized innovations are normally distributed with zero mean and unit variance [14]. The FDE requires the designer to set a false alarm probability. This is the probability that a non-erroneous measurement is rejected. Thus information that could have been useful is rejected. From this probability, a threshold is calculated by selecting a scaling on the normal distribution standard deviation to exclude the false alarm probability as shown in Figure 5.6. By decreasing the false alarm probability, the threshold increases and fewer outlier measurements will be rejected. The value used in this

work was 3, suggested from [14] to include 99.73 % of genuine measurements. This value corresponds to a false alarm probability of 0.27 %, which is relatively high. However, since this is a snapshot method, the effect of rejecting a good measurement would only affect a single epoch.

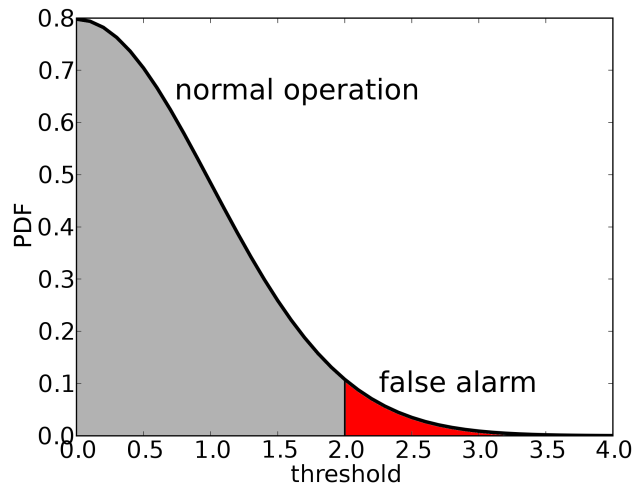


Figure 5.6: Fault Detection and Exclusion Threshold Selection

5.4 Summary

This chapter details the methods investigated to compensate for the errors inherent in general GPS operation and in operation in shadowed environments. For normal GPS operation, the code differential and carrier smoothed methods were presented. However, for short baselines the performance of the code differential algorithm is not greatly improved over position differencing due to the magnification of noise and unmodeled errors in the double difference generation. The carrier smoothed code method was presented as an improved positioning method for general operation. Also, this smoothing technique can be

adapted to other cases where pseudorange measurements are used. This decreases the noise in the range measurement for improved performance. However, these techniques are not viable in shadowed environments since satellite visibility is compromised and large multipath changes cannot be differentially corrected. In heavy foliage, the likelihood of both rover and base receivers accurately tracking at least five common satellites is low. As an alternative to differential operation, the low-level coupling architectures were described and compared. The loosely coupled method has disadvantages similar to the differential techniques; namely, satellite visibility can cause the corrections to be unavailable. The closely coupled method overcomes this difficulty by using any raw GPS observables from visible satellites. Therefore it is capable of supplying corrections even in low satellite visibility situations. Alternatively, a tightly coupled method was described but its requirement for special GPS equipment make it more difficult to implement, and therefore it is not explored further in this thesis. In addition to coupling, a fault detection and exclusion method was used to increase the integrity of the system's solution. This is accomplished by rejecting measurements considered to be outliers by comparing the normalized innovation parameter to a pre-determined threshold.

CHAPTER 6

RESULTS

To test the system, a path was chosen to include clear and heavy foliage areas, shown in Figure 6.1. The route was located in Auburn, AL and began along a relatively clear roadway, shown in the top of Figure 6.2. This section allows for good initialization of the coupling filter. It also gives a segment for comparing all methods without dealing with the effects of shadowed environments. Near the southern portion of the path, the test included heavy foliage, shown at the bottom of Figure 6.2. This segment degraded signal accuracy and satellite visibility, even dropping to only one satellite being reported by the GPS receiver. This path was chosen to test the system in varying conditions and to compare the system with stand-alone GPS solutions.

6.1 Pseudorange Calculated Position

As a baseline comparison, only the reported L1 pseudoranges and satellite positions from broadcast ephemerides were used to calculate the receiver position. This method was described in detail in Section 2.4. Due to the foliage conditions, there were points at which no solution could be generated since too few satellites were reported. The overall position is shown in Figure 6.3, and a zoomed segment is shown in Figure 6.4 detailing the operational difficulties of using GPS in foliage environments. As is clear from Figures 6.3 and 6.4, this solution is unacceptable for position critical vehicle operations since position jumps of approximately 100 meters occur in several places. Notice these jumps also occur in the shadowed portion of the track located along the southern straight section.



Figure 6.2: Clear Sky and Heavy Foliage Environments Along Dynamic Path

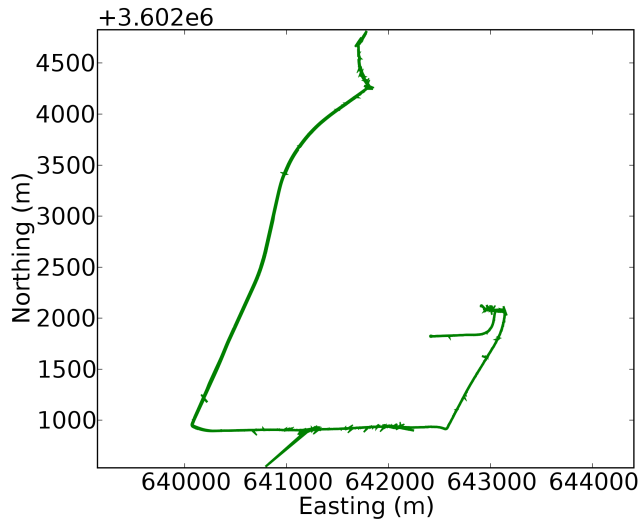


Figure 6.3: Pseudorange Calculated Positions

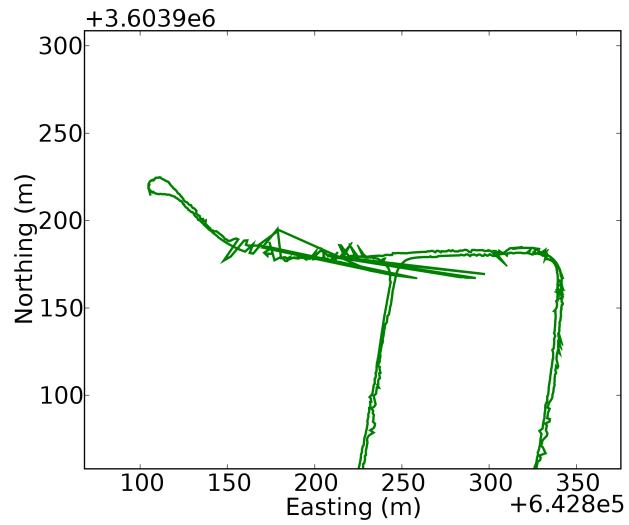


Figure 6.4: Zoom on Pseudorange Calculated Positions

The zoomed region shown in Figure 6.4 shows one of the characteristic effects of GPS operation in shadowed environments. As a heavily shadowed satellite drops in and out of visibility, it causes distinct spikes to be generated in a consistent direction. The magnitude of these jumps is large indicating the large amount of shadowing affecting the receiver in this area.

6.2 Closely Coupled Implementation Results

Using the closely coupled algorithm (described in Section 5.2) by including the IMU allows the navigation system to bridge GPS signal degradation. For this implementation, an automotive-grade IMU (Crossbow 440) was used. This method also increases the system solution rate to 50Hz, which is beneficial for vehicle control. The solution improves over the pseudorange position since the effect of jumps due to foliage is filtered out, as seen in Figure 6.5. The inclusion of the IMU in the filter allows the navigation system to remain on the path even though the shadowing effects would cause the solution to jump away from the path.

However, the solution still suffers from position and velocity jumps due to tree cover errors on the GPS measurements. These appear due to the innovation outliers, and their effect can be seen along the straight southern portion of the path shown in Figure 6.6. At the western jump, a satellite is reported at a single time epoch, and its innovation is large compared to the other measurements (magnitude of ≈ 7 compared to < 2). In this case the pseudorange measurement does not introduce the jump. The error occurs in the pseudorange rate measurement. This fault causes erroneous corrections to be made to the velocity in the navigation filter. This velocity then propagates to the jump in position

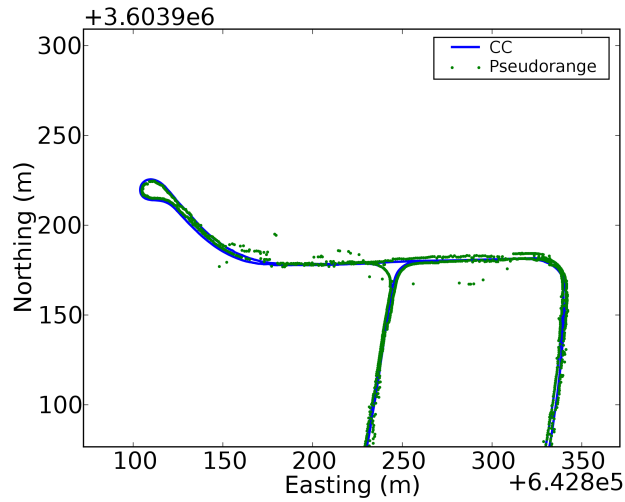


Figure 6.5: Zoom on Closely Coupled Positions

solution which is corrected over time. This is shown as the stepping in Figure 6.6 where the introduced velocity error causes the position solution to diverge over time before it is corrected.

6.3 Closely Coupled with FDE Implementation Results

By including the normalized innovation monitoring described in Section 5.3, these erroneous jumps are removed as shown in Figure 6.7. This implies that the correct outlier was detected and removed from the solution. As can be seen, this system is able to bridge parital signal loss while still estimating state corrections. In this case, the pseudorange rate innovation causes a spike in the normalized innovation parameter corresponding to a shadowed signal. The effects of this spike are removed, and operation is continued without that measurement. These results show the method is quite robust for operation in foliage environments like those encountered in the test path.

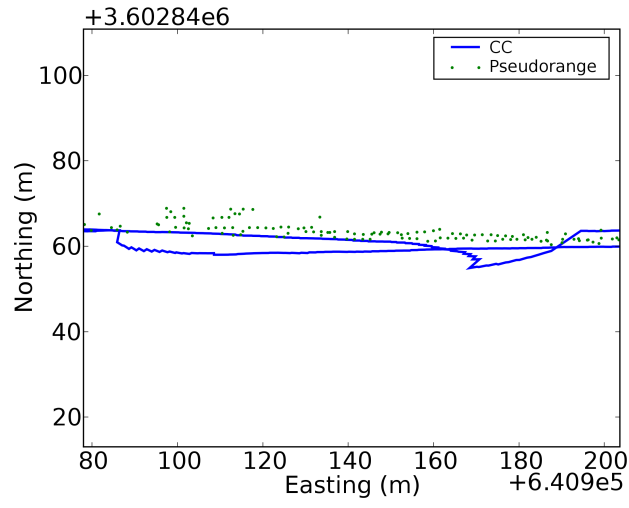


Figure 6.6: Comparison of Closely Coupled and Pseudorange Solutions

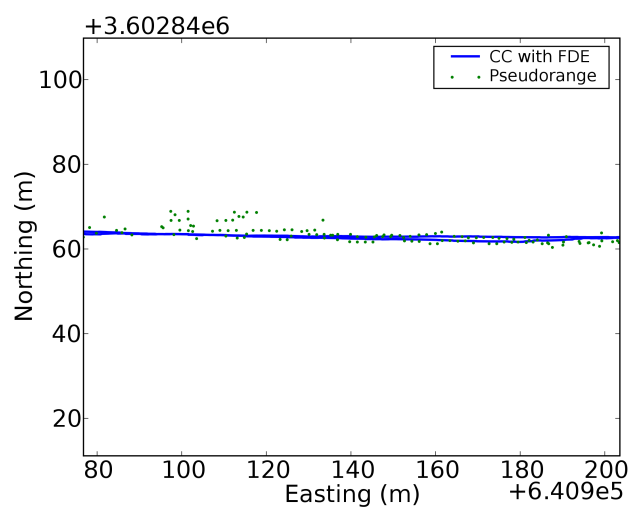


Figure 6.7: Comparison of Closely Coupled with FDE and Pseudorange Solutions

The normalized innovations are shown for the entire path as well as this portion of the path in Figures 6.8 and 6.9.

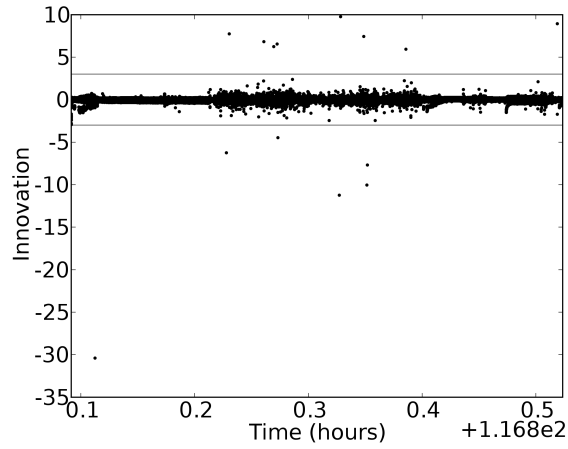


Figure 6.8: Normalized Innovations Over Entire Path

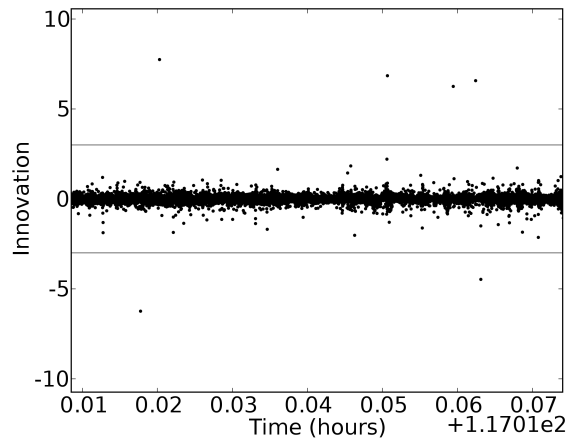


Figure 6.9: Normalized Innovations Over Zoom Segment

These plots show the threshold and the distribution of the normalized innovations. It is noted that during the middle portion of Figure 6.8, the shadowing effects are seen as a

spreading of the normalized innovations. The innovation thrown out at the beginning of Figure 6.9 is the one that causes the jump at the left part of Figure 6.6.

6.4 Comparison of Methods

To compare the methods of operation in shadowed environments, the paths for each method are plotted together above aerial photography via [1] in Figures 6.10 thru 6.12. As can be seen, the pseudorange positions are subject to large jumps in solution in foliage areas and even some jumps in clear sky areas. The GPS/INS closely coupled solution filters these jumps but also introduces jumps of lower magnitude since poor GPS measurements are still used in the navigation EKF. However, these jumps are removed with the FDE technique as seen in Figure 6.7.

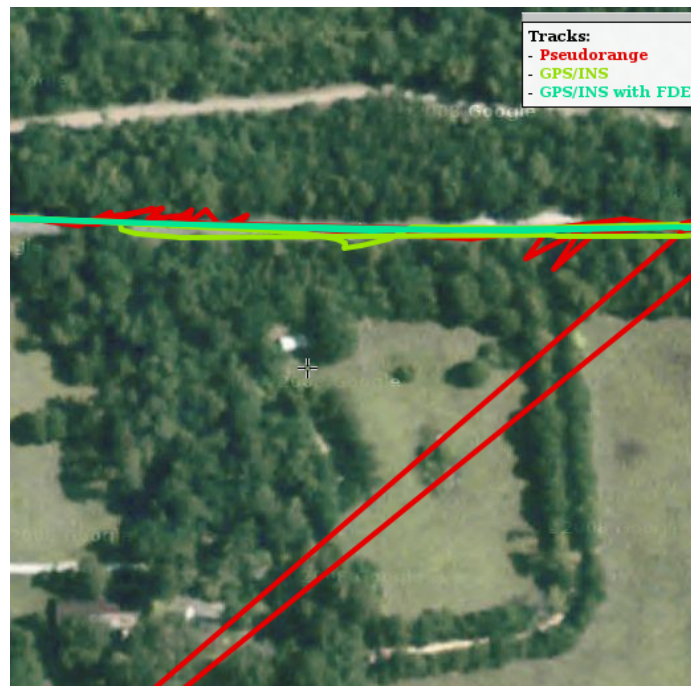


Figure 6.10: Overlay of Positioning Methods In Heavy Foliage

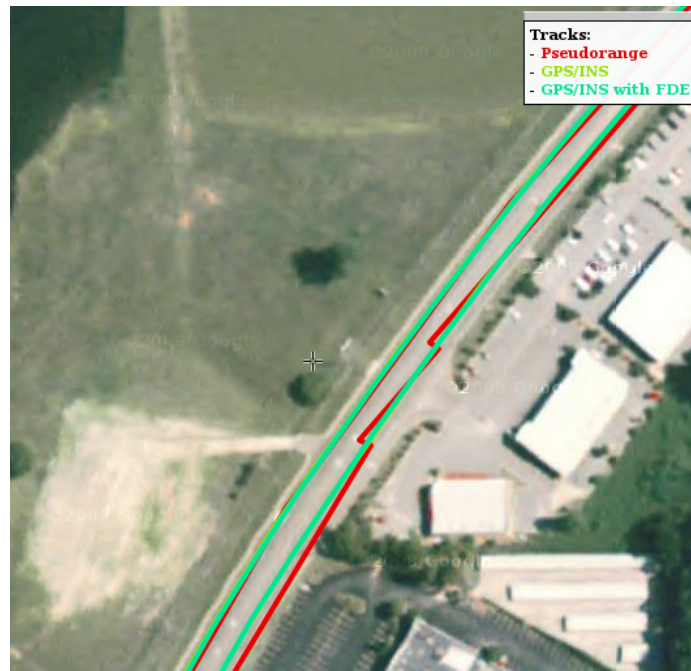


Figure 6.11: Overlay of Positioning Methods In Clear Sky

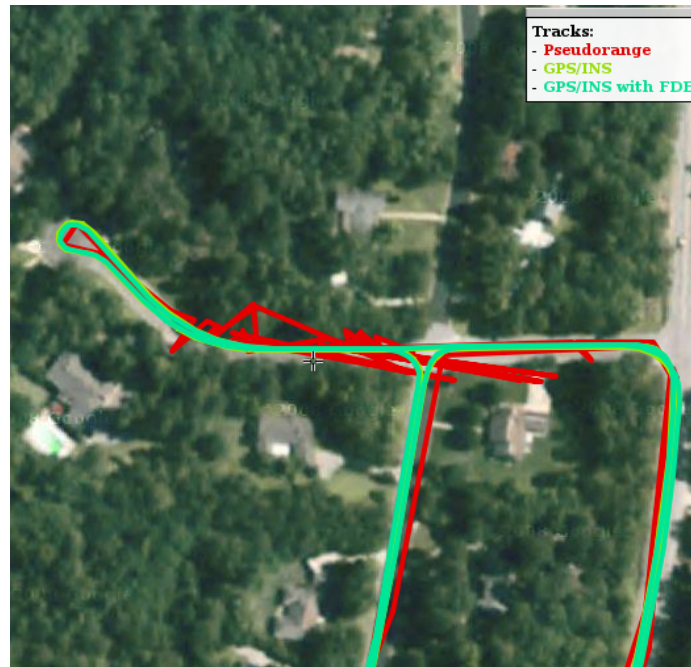


Figure 6.12: Overlay of Positioning Methods In Light Foliage

6.5 Summary

In this chapter, implementation results are presented for the closely coupled system with and without fault detection and exclusion described in Chapter 5. Comparison is made to stand-alone GPS operation by calculating pseudorange positions at every measurement update, wherever enough information was available. It is shown that the FDE method aids in navigation due to its removal of error-causing outliers in the measurement domain.

CHAPTER 7

CONCLUSION

This thesis has shown that GPS operation in shadowed environments such as heavy foliage poses diverse challenges. Although GPS receivers are subject to various error sources from satellite, atmospheric, and local effects, shadowed environments add complexity to the signal degradation. The work presented in this thesis develops a method of analysis for the errors specific to shadowed environments, namely the rapidly changing multipath and the signal attenuation caused by signal degradation. These sources of error affect the ability of a receiver's tracking loops to effectively track the incoming signal and thus negatively impact the receiver's performance in generating measurements. By using the error monitoring parameters ($M1$ and C/N_0) described in Chapter 4, the effects of these error sources can be tracked and visualized. This method makes error analysis more efficient than attempting to accurately determine the exact range error effects to which the GPS receiver is subject. A visualization technique for both a single satellite signal and for all satellites in view was developed to aid in the analysis of GPS operation in heavy foliage environments. As was shown in Chapter 4, the presence of foliage between the GPS receiver and the broadcasting satellite causes quickly varying and spontaneous drops in signal strength and also large changes in the signal multipath. The occurrence of these errors was seen to correspond to each other. This analysis led to the conclusion that foliage effects on the GPS signal was a quickly changing error mode and thus a snapshot method of fault detection could be used.

With insight into the errors affecting navigation operation, methods were detailed to handle such cases in Chapter 5. These methods included differential operation and inertial sensor integration. The performance of code-phase differential methods were compared and their shortcomings in shadowed environment operation described. Three integration methods (loosely coupled, closely coupled, and tightly coupled) were described and their advantages and shortcomings compared for operation in foliage. The closely coupled implementation was chosen since this architecture makes use of all available GPS observables along with the outputs of an IMU mechanization. This level of integration allows for operation in lower satellite visibility, which is common in shadowed environments. Comparison of the closely coupled navigation system with raw GPS processing (independent of other sensors) showed that integration reduced the large erroneous jumps in the navigation solution by combining GPS measurements with an INS calculated solution. It was also shown in Chapter 5 that the closely coupled architecture alone could not operate effectively in a shadowed environment. Due to the nature of the foliage-specific errors, a snapshot innovation filtering scheme was presented that allowed for normalized outlier rejection to add integrity to the navigation solution. Inclusion of the fault detection and exclusion (FDE) method further improved the operation of the navigation system during particularly dense foliage cover.

7.1 Future Work

The next step in this research is to package the algorithms and hardware into a deployable module for use on actual systems. This platform has been investigated and advances will be forthcoming.

Further analysis of the multipath effects could improve the processing by allowing the navigation processor to estimate these errors. Therefore rejection could be avoided by removal of these error sources. Improved multipath monitoring could also be extended to other applications such as more advanced differential processing methods like real-time kinematic (RTK). This improvement would be beneficial since local effects are errors that differential methods cannot intrinsically remove.

The navigation methods presented in this thesis can also be improved upon by adding more sophisticated integrity monitoring schemes to the processing. With these statistical techniques, more explicit bounds on the system integrity would be available. Therefore the bounding thresholds could be set as a function of desired performance. Further performance improvement would come by using a receiver capable of accepting aiding for signal tracking. This could be developed as part of a software receiver platform as this functionality is not available to receivers used in Auburn's GPS and Vehicle Dynamics Laboratory.

BIBLIOGRAPHY

- [1] *Gps visualizer*, <http://www.gpsvisualizer.com/>.
- [2] *National geodetic survey precise gps orbits*, <http://www.ngs.noaa.gov/orbits/>.
- [3] Bhamer, *Ionosphere*, <http://en.wikipedia.org/wiki/Ionospherevg>, May 2007.
- [4] Sunil B. Bisnath and Richard B. Langley, *Pseudorange multipath mitigation by means of multipath monitoring and de-weighting*, Proceedings of KIS 2001 (Banff, Alberta), June 2001.
- [5] Michael H. Bruch, G.A. Gilbreath, J.W. Muelhauser, and J.Q. Lum, *Accurate waypoint navigation using non-differential gps*, Tech. report, Space and Naval Warfare Systems Center, 2002.
- [6] Rob Conley, Ronald Cosentino, Christopher J. Hegarty, Elliott D. Kaplan, Joseph L. Leva, Maarten Uijt de Haag, and Karen Van Dyke, *Performance of stand-alone gps*, Understanding GPS: Principles and Applications (Elliott D. Kaplan and Christopher J. Hegarty, eds.), Artech House, 2006.
- [7] Arinc Research Corporation, *Navstar interface control document*, <http://www.navcen.uscg.gov/gps/geninfo/IS-GPS-200D.pdf>, April 2000.
- [8] Tom Creel, Arthur J. Dorsey, Philip J. Mendicki, Jon Little, Richard G. Mach, and Brent A. Renfro, *New, improved gps: The legacy accuracy improvement initiative*, GPS World (2006).
- [9] Donghai Dai, Todd Walter, C.J. Comp, Y.J. Tsai, P.Y. Ko, Per Enge, and J. David Powell, *High integrity multipath mitigation techniques for ground reference stations*, Proceedings of the 1997 ION GPS Conference, 1997.
- [10] Nicholas J. DeCesare, John R. Squires, and Jay A. Kolbe, *Effect of forest canopy on gps-based movement data*, Wildlife Society Bulletin **33** (2005), no. 3, 935–941.
- [11] Jay A. Farrell and Matthew Barth, *The global positioning system & inertial navigation*, McGraw-Hill, 1998.
- [12] Julio C. Farret and Marcelo C. Santos, *An alternative method for detection and mitigation of static multipath in l1 carrier phase measurements*, Proceedings of the ION NTM 2001, 2001.
- [13] Garmin, *Gps glossary*, <http://www8.garmin.com/aboutGPS/glossary.html>, 2008.

- [14] Paul D. Groves, *Principles of gnss, inertial, and multisensor integrated navigation systems*, Artech House, 2008.
- [15] Christopher R. Hamm, IV Warren S. Flenniken, David M. Bevly, and Daniel E. Lawrence, *Comparative performance analysis of aided carrier tracking loop algorithms in high noise/high dynamic environments*, Proceedings of the ION GNSS (Long Beach, CA), ION, September 2004.
- [16] Hisashi Hasegawa and Tetsuhiko Yoshimura, *Estimation of gps positional accuracy under different forest conditions using signal interruption probability*, Journal of Forestry Research **12** (2007), 1–7.
- [17] Stephen Hilla, *Plotting pseudorange multipath with respect to satellite azimuth and elevation*, GPS Solutions **8** (2004), 44–48.
- [18] J. J. Spilker Jr., *Foliage attenuation for land mobile users*, Global Positioning System: Theory and Application, Volume 1, American Institute of Aeronautics and Astronautics, Inc., 1996.
- [19] ———, *Gps navigation data*, Global Positioning System: Theory and Applications, Volume 1 (Bradford W. Parkinson and James J. Spilker Jr., eds.), American Institute of Aeronautics and Astronautics, Inc., 1996.
- [20] ———, *Satellite constellation and geometric dilution of precision*, Global Positioning System: Theory and Application, Volume 1, American Institute of Aeronautics and Astronautics, Inc., 1996.
- [21] Elliott D. Kaplan and Christopher J. Hegarty (eds.), *Understanding gps: Principles and applications*, Artech House, 2006.
- [22] G. Lachapelle, J. Hendriksen, and T. Melgara, *Seasonal effect of tree foliage on gps signal availability and accuracy for vehicular navigation*, Proceedings of the 7th International Technical Meeting of The Satellite Division of the Institute of Navigation (Salt Lake City, UT), September 1994, pp. 527–532.
- [23] David Gary Lawrence, *Aircraft landing using gps*, Phd dissertation, Stanford University, September 1996.
- [24] Helena Leppakoski, Heidi Kuusniemi, and Jarmo Takala, *Raim and complementary kalman filtering for gnss reliability enhancement*, Proceedings of the PLANS Conference, 2006.
- [25] Pratap Misra and Per Enge, *Global positioning system: Signals, measurements, and performance*, second ed., Ganga-Jamuna Press, 2006.
- [26] Dignus-Jan Moelker, *Multiple antennas for advanced gnss multipath mitigation and multipath direction finding*, Proceedings of ION GPS-97, September 1997.

- [27] Bradford W. Parkinson, *Gps error analysis*, Global Positioning System: Theory and Application, Volume 1 (Bradford W. Parkinson and James J. Spilker Jr., eds.), American Institute of Aeronautics and Astronautics, Inc., 1996.
- [28] Bradford W. Parkinson and Per K. Enge, *Differential gps*, Global Positioning System: Theory and Application, Volume 2 (Bradford W. Parkinson and James J. Spilker Jr., eds.), American Institute of Aeronautics and Astronautics, Inc., 1996.
- [29] C. Rocken, C. Meertens, B. Stephens, J. Braun, T. VanHove, S. Perry, O. Rudd, and M. McCallum and J. Richardson, *Unavco academic research infrastructure (ari) receiver and antenna test report*, Tech. report, UNAVCO, 1996.
- [30] P. Sigrist, P. Coppin, and M. Hermy, *Impact of forest canopy on quality and accuracy of gps measurements*, Int. J. Remote Sensing **20** (1999), no. 18, 3595–3610.
- [31] Robert F. Stengel, *Optimal control and estimation*, Dover Publications, 1994.
- [32] Byron D. Tapley, Bob E. Schutz, and George H. Born, *Statistical orbit determination*, Elsevier Academic Press, 2004.
- [33] William Travis, Robert Daily, David M. Bevly, Kevin Knoedler, Reinhold Behringer, Hannes Hemetsberger, Jrgen Kogler, Wilfried Kubinger, and Bram Alefs, *Sciautronics-auburn engineering's low-cost high-speed atv for the 2005 darpa grand challenge*, Journal of Field Robotics **23** (2006), no. 8, 579–597.
- [34] United States Naval Observatory (USNO), *Gps constellation status*, <ftp://tycho.usno.navy.mil/pub/gps/gpstd.txt>.
- [35] Phillip W. Ward, John W. Betz, and Christopher J. Hegarty, *Gps satellite signal characteristics*, Understanding GPS: Principles and Applications (Elliott D. Kaplan and Christopher J. Hegarty, eds.), Artech House, 2006.
- [36] ———, *Satellite signal acquisition, tracking, and data demodulation*, Understanding GPS: Principles and Applications (Elliott D. Kaplan and Christopher J. Hegarty, eds.), Artech House, 2006.
- [37] IV Warren S. Flenniken, *Modeling inertial measurement units and analyzing the effect of their errors in navigation applications*, Master's thesis, Auburn University, December 2005.
- [38] Hayati Zengin and Ahmet Yesil, *Comparing the performances of real-time kinematic gps and a handheld gps receiver under forest cover*, Tech. report, Istanbul University, Faculty of Forestry, Department of Forest Management Planning, 2004.

NOMENCLATURE

\bar{x}	generic vector
ϵ_s	pseudorange error for satellite s
ϵ_{sl}	pseudorange error for satellite s and L-band frequency l
η_{sl}	carrier phase error for satellite s and L-band frequency l
λ	longitude angle
λ_l	carrier wavelength for L-band frequency l
ϕ	latitude angle
ϕ_{sl}	carrier phase measurement for satellite s and L-band frequency l
ρ_s	pseudorange from user to satellite s
$c\delta t_{u,s}$	clock offset of user, satellite
c	speed of light
e	Earth-Centered Earth-Fixed (ECEF) coordinate frame
e	body coordinate frame
i	inertial coordinate frame
$I_{s1,2}$	ionospheric delay on L1, L2 frequency for satellite s
$M\phi_{sl}$	carrier phase multipath for satellite s and L-band frequency l

$M\rho_{sl}$	pseudorange multipath delay for satellite s and L-band frequency l
n	navigation coordinate frame
N_{sl}	carrier phase integer ambiguity for satellite s and L-band frequency l
$r_{eb,es}^e$	ECEF position vector of user, satellite
$r_{eb,es}$	user, satellite distance from ECEF origin
r_{eb}	user range to ECEF origin
r_{sb}	range from satellite to user
s	satellite coordinate frame
t_m	time a signal is measured
T_s	tropospheric delay for satellite s
t_s	time a signal leaves the satellite
$x_{\beta\gamma}^\alpha$	x vector from β origin to γ origin expressed in α coordinates
$x_{\beta\gamma}$	magnitude of x vector from β origin to γ origin
$x_{eb,es}$	ECEF x coordinate of user, satellite
$y_{eb,es}$	ECEF y coordinate of user, satellite
$z_{eb,es}$	ECEF z coordinate of user, satellite

APPENDIX A

COORDINATE FRAMES AND TRANSFORMATIONS

Part of navigation solution presentation is a clear understanding of what coordinate frames are being used. Also, transformations between these coordinate systems make the combination of different system types (like GPS and INS) compatible. A description of the frames used in this work is given followed by conversions between them used in this work.

A.1 Coordinate Frames

It is necessary to clearly delineate what coordinate frame system is being used and what frame measures are related to. This is particularly important in combining systems that give values of the same quantity in different frames.

A.1.1 Earth-Centered Inertial (ECI) Frame

The ECI frame is approximately an inertial frame, meaning it can be sufficiently approximated as a non-rotating coordinate frame. This is not strictly true but for the purposes of the calculations used, it can be approximated as such. The necessity of describing this frame is that this is the reference system to which inertial sensors measure. The origin of the ECI frame is located at the center of the Earth. Its z axis is coincident with the Earth's axis of rotation. The x axis points in a non-rotating direction, usually taken to be the vernal equinox [14]. The y axis completes the right-handed coordinate system. This frame is illustrated in Figure A.1.

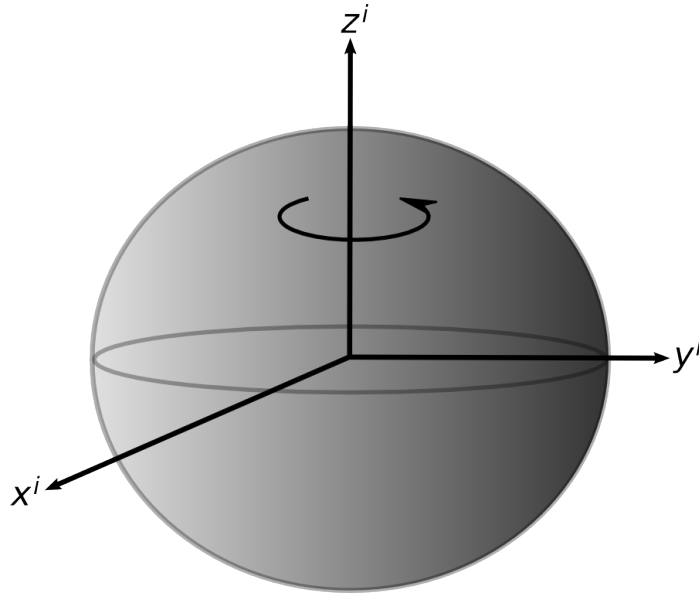


Figure A.1: Earth-Centered Inertial (ECI) Frame

A.1.2 Earth-Centered Earth-Fixed (ECEF) Frame

The ECEF frame is a frame in which the origin is the center of the earth, the z axis is coincident with the Earth's axis of rotation, the x axis points along 0° longitude, and the y axis completes the right-handed coordinate system by pointing along 90° longitude. This frame is illustrated in Figure A.2.

A.1.3 Navigation Frame

The local navigation frame is defined with an origin on the user body (usually center of mass or sensor coordinate system center). It is the point for which the navigation solution is sought [14]. One axis points toward the local North direction, co-planar with the ECEF z axis. The Down direction is defined to be perpendicular to the Earth ellipsoid in the direction of the center of the Earth. The East direction completes the right-hand coordinate

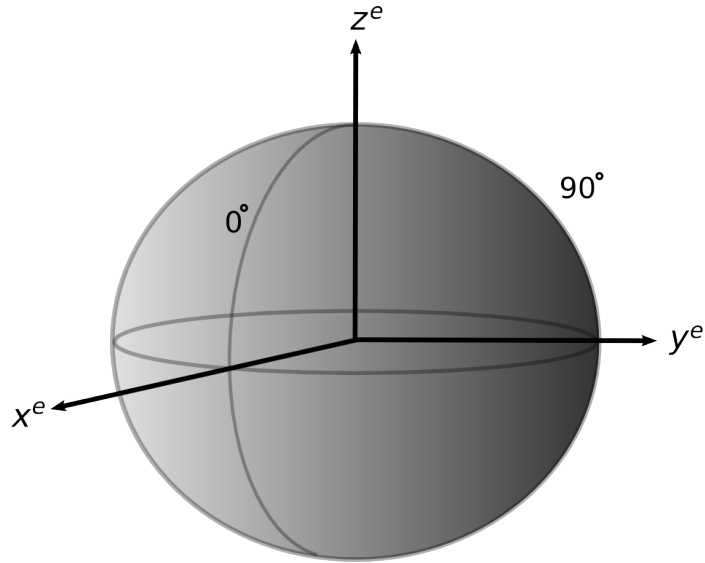


Figure A.2: Earth-Centered Earth-Fixed (ECEF) Frame

system. This frame is illustrated in Figure A.3. Note that there are singularities for this frame at each pole because of the nature of the North direction definition.

A.1.4 Body Frame

The body frame is the frame rigidly attached to the user body (assumed to be coincident with the sensor coordinate system). The x axis points in the forward direction of the body, the z axis downward on the body, and the y axis completes the right-hand coordinate system. This frame is illustrated in Figure A.4.

A.1.5 Orbit Frame

The orbit frame is a planar system with the origin at the Earth's center and inclined from the polar axis by an inclination angle, i , as shown in Figure A.5. This frame is also rotated about the polar axis by Ω , the longitude of the ascending node. The ascending node

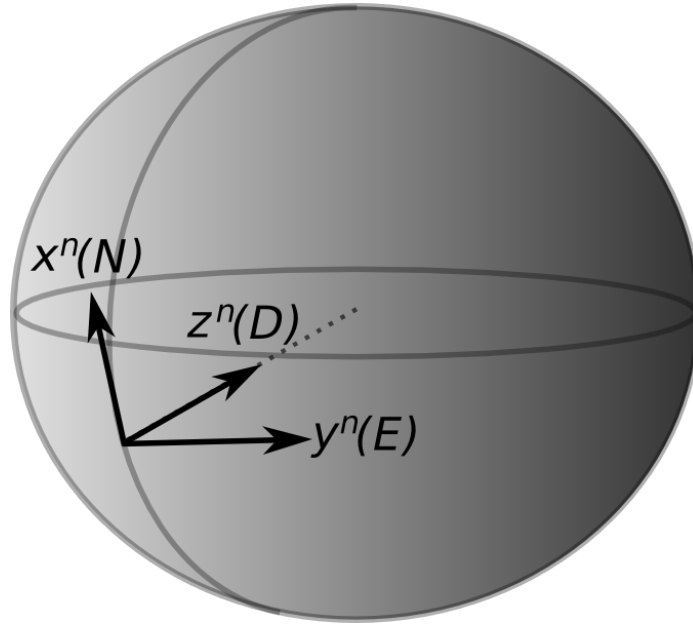


Figure A.3: Navigation Frame

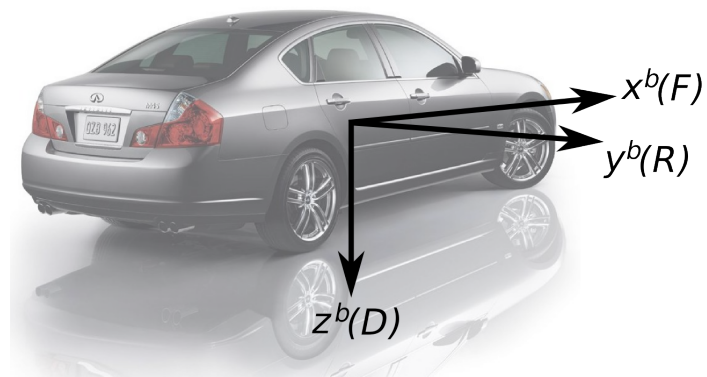


Figure A.4: Body Frame

is the point at which a satellite in the orbit crosses the equatorial plane in the positive z direction. This angle is measured from the IERS reference meridian as shown in Figure A.5 [14]. Within the orbit plane, the x axis is defined from the Earth center to the ascending

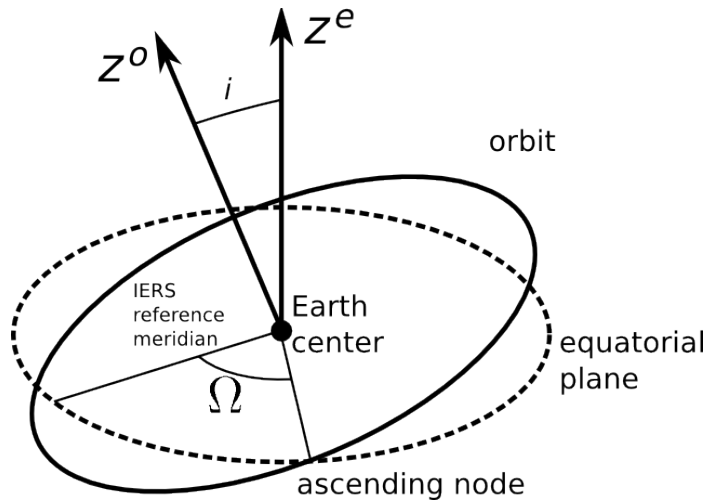


Figure A.5: Orbital Plane With Respect To Equatorial Plane

node and the y axis completes the right-hand coordinate system as shown in Figure A.6. The orientation of the plane is defined by the argument of perigee, ω . The perigee is the point of closest approach in the orbit.

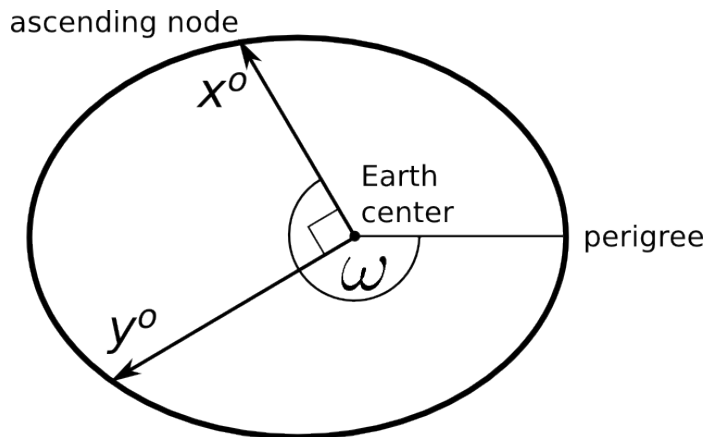


Figure A.6: Orbit Frame

A.1.6 Satellite Frame

The satellite frame is defined for satellite s as the coordinate frame centered at the phase center of the satellite antenna. Due to its use in this work, directions of the coordinate axes are not important since the origin location is the only important set of coordinates to be determined.

A.2 Coordinate Transformations

Transformation between sets of coordinate frames is necessary since various quantities used in the implementation are measured or given in different coordinate frames. Also, the user may need the resulting coordinates in a more usable form for their application. For example, ECEF coordinates are not as helpful as navigation coordinates for vehicle operation. Also, most mapping applications use geodetic coordinates since the origin of the navigation coordinates is difficult to correlate with positions on the Earth's surface.

A.2.1 Coordinate Transformation Matrix

In order to relate the various coordinate frames, a transformation matrix is used. To take a vector quantity between two coordinate frames δ and γ that is expressed in coordinate frame α , $x_{\delta\gamma}^\alpha$, to be expressed in coordinate frame β , $x_{\delta\gamma}^\beta$ can be accomplished by

$$x_{\delta\gamma}^\beta = C_{\alpha}^{\beta} x_{\delta\gamma}^\alpha \quad (\text{A.1})$$

The inverse operation is accomplished by using the transpose of the transformation matrix, that is

$$C_{\beta}^{\alpha} = \left(C_{\alpha}^{\beta}\right)^T \quad (\text{A.2})$$

If an angular rate vector is expressed in skew-symmetric form then it can be transformed to another coordinate frame as

$$\Omega_{\beta\alpha}^{\delta} = C_{\gamma}^{\delta} \Omega_{\beta\alpha}^{\gamma} C_{\delta}^{\gamma} \quad (\text{A.3})$$

The rate of change of the transformation matrix is found as

$$\dot{C}_{\beta}^{\alpha} = C_{\beta}^{\alpha} \Omega_{\alpha\beta}^{\beta} \quad (\text{A.4})$$

A.3 ECEF and Geodetic Coordinates

To translate between ECEF coordinates and geodetic coordinates, the Earth's ellipsoidal model must be used. For these transformations, the transverse radius of curvature, R_E , is needed. This is the radius of curvature of constant latitude lines calculated as

$$R_E(L_b) = \frac{R_0}{\sqrt{1 - e^2 \sin^2 L}} \quad (\text{A.5})$$

where R_0 is the equatorial radius and L_b is the geodetic latitude. Therefore ECEF coordinates can be calculated from geodetic coordinates as

$$x_{eb}^e = (R_E(L_b) + h_b) \cos L_b \cos \lambda_b \quad (\text{A.6})$$

$$y_{eb}^e = (R_E(L_b) + h_b) \cos L_b \sin \lambda_b \quad (\text{A.7})$$

$$z_{eb}^e = \left[(1 - e^2) R_E(L_b) + h_b \right] \sin L_b \quad (\text{A.8})$$

and geodetic coordinates can be calculated from ECEF coordinates as

$$\begin{aligned} \sin L_b &= \frac{z_{eb}^e}{(1 - e^2) R_E(L_b) + h_b} \\ \tan \lambda_b &= \frac{y_{eb}^e}{x_{eb}^e} \\ h_b &= \frac{\sqrt{(x_{eb}^e)^2 + (y_{eb}^e)^2}}{\cos L_b} - R_E(L_b) \end{aligned} \quad (\text{A.9})$$

This solution has to be iterated through since R_E is a function of latitude, and latitude and height must be solved for iteratively.